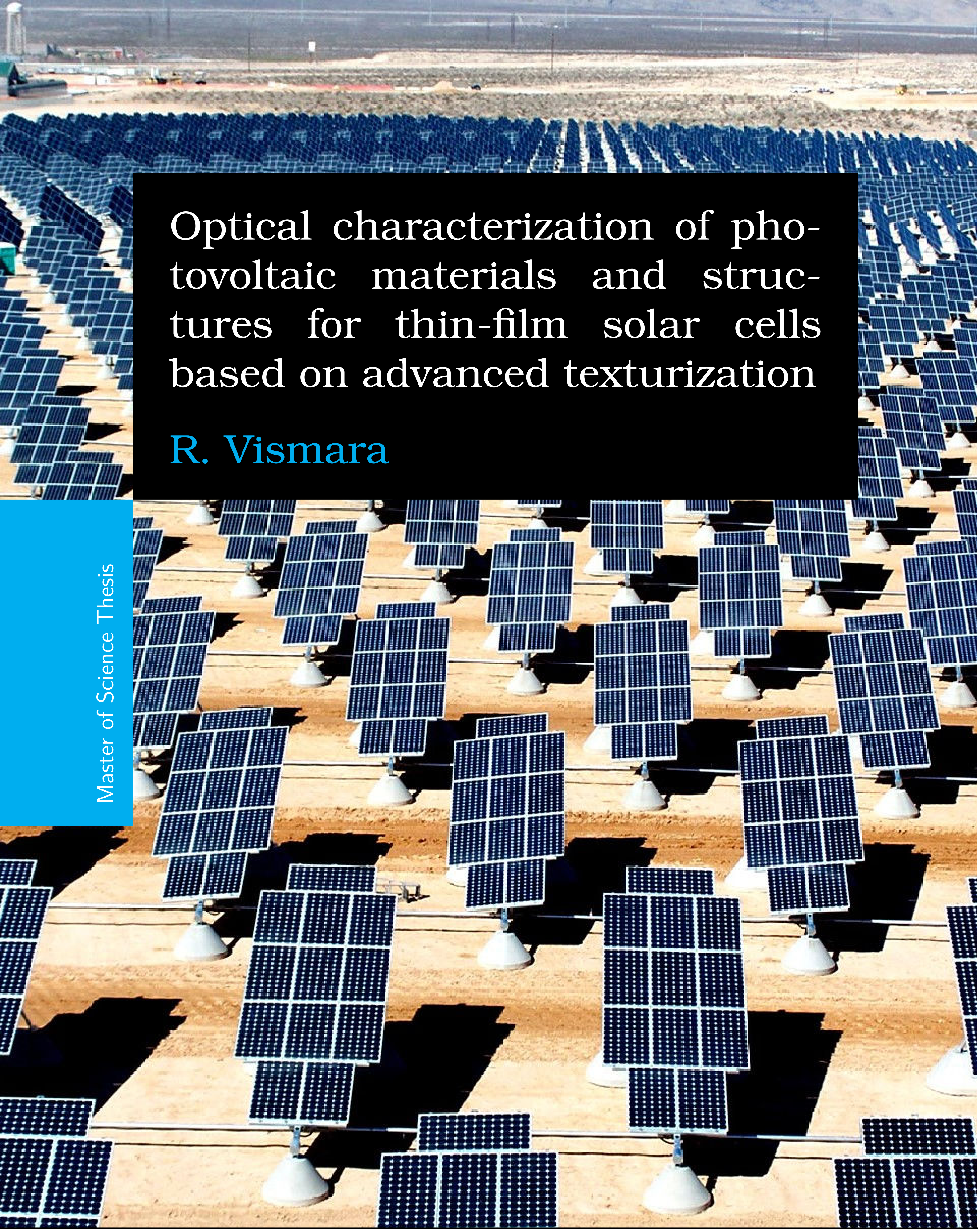

Optical characterization of photovoltaic materials and structures for thin-film solar cells based on advanced texturization

R. Vismara

Master of Science Thesis

Optical characterization of photovoltaic materials and structures for thin-film solar cells based on advanced texturization

MASTER OF SCIENCE THESIS

For the degree of Master of Science in Sustainable Energy Technology (SET) at Delft University of Technology

R. Vismara

Wednesday, 10^{th} September 2014

Faculty of Applied Science (AS) · Delft University of Technology

DELFT UNIVERSITY OF TECHNOLOGY
DEPARTMENT OF
PHOTOVOLTAIC MATERIALS AND DEVICES (PVMD)

The undersigned hereby certify that they have read and recommend to the Faculty of Applied Science (AS) for acceptance a thesis entitled

OPTICAL CHARACTERIZATION OF PHOTOVOLTAIC MATERIALS AND STRUCTURES FOR THIN-FILM SOLAR CELLS BASED ON ADVANCED TEXTURIZATION

by

R. VISMARA

in partial fulfillment of the requirements for the degree of

MASTER OF SCIENCE SUSTAINABLE ENERGY TECHNOLOGY (SET)

Dated: Wednesday, 10^{th} September 2014

Supervisor(s): Dr. O. Isabella

Reader(s): Dr. O. Isabella

Prof.Dr. M. Zeman

Dr. O. El Gawhary

Abstract

Advanced texturization is a promising approach to increase the performance of thin-film solar cells. Currently, light trapping schemes implemented in state-of-the-art devices utilize randomly textured interfaces to increase their optical performance. Periodic gratings, however, have the potential to outperform their random counterparts and are thus of great interest for PV applications. In this work, an analysis of the optical performance of different advanced grating concepts applied to thin-film solar cells is presented. Different types of absorber materials were taken into account: amorphous and micro-crystalline silicon, crystalline silicon and Copper-Indium-Gallium-diSelenide chalcopyrite semiconductors.

In the first part of this work, the materials employed in thin-film silicon- and CIGS-based devices were characterized. The appropriate equipment and fitting models were used, in order to obtain reliable optical properties. This characterization phase involved samples of absorber and supporting layer materials, which were provided by partners of the Photovoltaic Materials and Devices group. The outcome of this characterization was compared with the results obtained by the sample manufacturers, to ensure the reliability of the properties extracted.

After the characterization, the analysis of the optical performance of different advanced texturizations was carried out, by means of optical simulations. The first part consisted of a study of one-dimensional asymmetric periodic gratings, applied to amorphous silicon, micro-crystalline silicon, and CIGS standard thin-film cells. The optical properties of materials used in the simulations were obtained from the previous characterization phase. Results showed a better performance of asymmetric gratings with respect to symmetric ones, and for each cell type the optimal grating geometrical dimensions were found. In addition to the grating optimization, an analysis of the structure optical performances using different materials was done. This second investigation showed that the utilization of more transparent materials further improves the cell optical behaviour. In this way, it was possible to determine the performance limit (in terms of generated photocurrent density) achievable by the three different cell types with 1-D periodic textures.

The last step of this work involved the study of the optical performance of crystalline silicon thin-film cells based on elongated nano-structures (nanowires). First, the analysis of light propagation inside the solar cell showed a resonant behaviour induced by the presence of nanowires. This resonances result in an absorptance increase (with respect to equivalent flat devices), particularly in the near infra-red region of the spectrum. Following the analysis of light propagation behaviour, the effect of the nanowire geometrical dimensions was investigated. The impact of the elongated nano-structure height and diameter was observed, and the optimal configuration of the cell was determined. Finally, the performance of the cell under different light illumination conditions was analysed. Results showed that nanowire-based silicon solar cells can achieve constant high absoptance values in a wide range of light angles of incidence, property that can allowe them to achieve better performance in a wide range of illumination conditions.

Table of Contents

List of Figures

List of Tables

Preface

This document is a part of my Master of Science graduation thesis in Sustainable Energy Technology (SET) at Delft University of technology. The work of this project was carried out inside the Photovoltaic Materials and Devices (PVMD) group, which is part of the faculty of Electrical Engineering, Mathematics and Computer Science at Delft University of Technology.

This report represents the conclusion of nine months of hard work carried out to complete my MSc student career. Looking back at this period, with all its ups and downs, I realize that achieving this result would have not been possible without the help of a great number of people. In particular, my first thank go to my parents, whose support and encouragement has been fundamental in all my life, but particularly in this last two years. To them I say: *grazie di tutto, senza il vostro aiuto e il vostro supporto adesso non sarei dove mi trovo, le parole non bastano per esprimere tutta la gratitudine che provo nei vostri confronti.* A big *thank you* goes also to my grandma, whose presence here close to me made me feel at home even when being more than 1000 km away from it. So: *hartstikke bedankt voor alles.*

I would also like to take this chance to say a big *thank you* to the new friends I made during the last two years. This experience to study in Delft has been one of the best of my life, and it would not have been the same without the presence of Daniel, Derk, Jessica, Julián, Steph and Timo: you really made this last couple of years unforgettable.

Furthermore, I would like to thank all the members of the PVMD group that helped me during the course of this project. First, a special *grazie* goes to my supervisor Dr. O. Isabella. His help, supervision and constant motivation were fundamental to achieve the results presented in this work, and I am sure that in the future it will be a pleasure to work once more under your supervision. I would also like to thank Prof. Dr. M. Zeman for welcoming me inside the PVMD group and for giving me the possibility to conduct my graduation project inside his group. A special thank you goes also to my colleagues Dane and Theodoros, who at various stage of this project have helped me to achieve the results. I would also like to thank all the technicians and research members of the PVMD group, which helped me in carrying out measurements or had suggestions on how to improve the work I was carrying out.

A special thank goes to Dr. O. El Gawhary, from the Optics Research Group of the Applied Science faculty at TU Delft, who accepted to be part of the defence committee of this thesis.

Finally, I would like to thank the researchers at Commissariat á l'Energie Atomique (CEA) and Forschungszentrum Jülich GmbH (FZJ), which are partners of the PVMD group in the AGATHA project, for providing the samples used in the characterization phase of this project.

“Look up at the stars and not down at your feet. Try to make sense of what you see, and wonder about what makes the universe exist. Be curious”

— *Stephen Hawking*

Chapter 1

Introduction

1-1 Background and motivation

During the last few years, the attention towards sustainability has constantly increased. The current fossil-fuel based economy has proven to be no longer sustainable, due to economical, political, and environmental concerns. The global demand of energy has more than doubled during the last 40 years (Figure 1-1), and the predictions show an expected increase of 50% with respect to the current situation [1]. This further raise in global consumption can be mostly attributed to developing countries, with countries like China and India and the Middle East region playing a major role among them [2].The constantly growing energy demand cannot be satisfied by currently-used non renewable energy sources, mainly fossil fuels (i.e. coal, oil, natural gas etc.), which at the present utilization rate will encounter a (relatively) quick depletion. Furthermore, the resources of oil and gas are concentrated in a small number of countries, which can result in instability of the energy prices (in addition to the probable price increase caused by the resources depletion); this instability could pose a threat to the worldwide energy supply security [3].

In addition to the aforementioned economical and political concerns [4], during the last few years the debate over the environmental consequences of the current fossil-fuel based economy has attracted more and more attention, mainly due to the observed global warming effects. According to the Intergovernmental Panel on Climate Change (IPCC), science now shows with a 95% certainty that human activity is the main driver in the global warming observed since the mid-20^{th} century [5]. The reason for these unprecedented changes to the climate can be ascribed to the increased concentration of greenhouse gasses (GHG) in the atmosphere during the last two centuries, since a strong correlation with the change in atmospheric and oceanic temperatures was found [5]; the greatest part of the anthropogenic GHG emissions is the result of burning fossil fuels in order to produce energy. Climate change requires urgent and drastic actions to be taken, in order to avoid serious consequences on a global scale.

It is therefore clear that a transition from a fossil-fuel based economy to a more sustainable one has become necessary. A great contribution to this transformation can be given by a large-scale implementation of renewable energies. Despite the rising awareness of the consequences

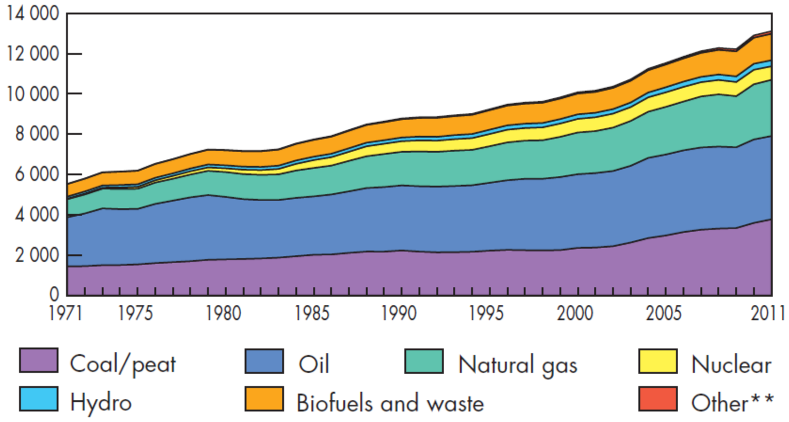

Figure 1-1: World total primary energy supply from 1971 to 2011 by fuel (in Mtoe) [6].

and concerns of fossil-fuel wide utilization and depletion, their employment has grown over the last decades (Figure 1-1), and so did the global investments related to them [7]. Renewable energy has also undergone a huge increase during the last years [8], but its contribution to the total energy production remains much too small with respect to fossil fuels (Figure 1-2). The result is that the doubling of global energy production witnessed during the last 40 years has caused a corresponding doubling of global GHG emissions, intensifying in this way the magnitude of global warming [6, 9]. Thus, although the growth of renewable energy in the last years has been evident, and in spite of the continuously growing investments in the renewable sector [7], a further increase of the utilization and the diffusion of renewables is necessary in order to mitigate the effects of climate change and reduce the depletion rate of fossil fuels, which will remain the main source of energy for the next decades [1, 7].

Among all types of renewable resources, solar energy has the greatest development potential, since it is the biggest energy source available on Earth [10]. In particular photovoltaics (PV), which is the direct conversion of solar irradiation into electricity, offers a great number of advantages: not only it is a technology that produces clean energy from an "*inexhaustible and mostly import-independent resource*" [11], but its capability to operate as a stand-alone system makes it the ideal solution, if combined with appropriate energy storage methods [12], for the electrification of rural areas which are not connected to the electricity grid.

In spite of the advantages, electricity production from solar energy was never able to economically compete with traditional technologies (coal and natural gas power plants, hydroelectricity generation etc.), mainly due to high production costs of solar panels; thus, the great growth of the PV sector witnessed during the last decade has been mainly driven by governments policies and feed-in tariffs [8, 11]. Only in recent years PV has reached the so-called *grid parity* without the aid of subsidies, in a wide variety of locations [13]; this happened mainly due to the huge drop in the production costs, which greatly reduced the retail price of panels (from an average cost in 2006 of 4.5 $\$/Wp$ to less than 1 $\$/Wp$ in 2011) [14]. To achieve a full competitiveness of PV energy worldwide (especially in those location where sun irradiation is lower) and to further reduce the price of electricity generated by PV modules, research is required to improve their conversion efficiency and reduce the material utilization, reducing in this way part of the production costs.

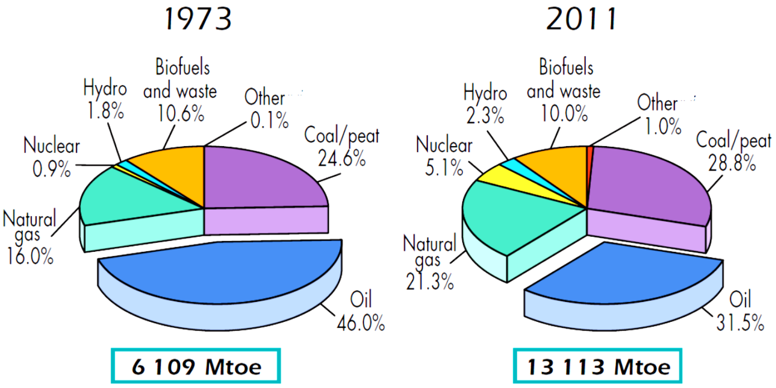

Figure 1-2: 1973 and 2001 fuel shares of the total primary energy supply. The voice *Other* includes geothermal, solar, wind, heat etc.[6].

1-2 History of photovoltaics

Since the photovoltaic effect was discovered, by the French physicist E. Becquerel in 1839 [15], the evolutio the PV sector witnessed has been great. From the first solar cell, built by C. Fritts in 1891 and made of selenium coated with gold, the technology gradually evolved until, in 1941, the first silicon (Si) solar cell was built by R. Ohl [16]. Since then, Si has become the most used material for the production of photovoltaic cells [17].

The current PV production consists of many different technologies, from wafer-based silicon to various thin-film approaches. The range of current and possible future technologies has been grouped (Figure 1-3) in 3 different generations [18]. The so called 1^{st} generation PV consists of single-junction solar cells based on silicon wafers, including single-crystal (c-Si) and multi-crystalline silicon (mc-Si). 1^{st} generation silicon PV greatly benefited from the possibility to use the same materials, the processing know-how and the manufacturing tools from the integrated circuit industry, and that allowed a rapid move to large-scale production [17]. The main drawbacks of these 1G technologies are the high amount of energy required for their production and the limited achievable efficiency of the cells, due to the single-junction approach [19]. Other disadvantages of 1^{st} generation PV, with respect to the other generations, are the higher material and production costs, but the drop they experienced in recent years [14] reduced this price gap between different generations.

1-2-1 2^{nd} generation PV

Currently, PV market is dominated by 1G technologies [14], which have already reached a price level that makes them economically competitive with non-renewable electricity production, as discussed in Section 1-1. However, since the great cost reduction that allowed photovoltaics to achieve grid parity only occurred very recently, alternative technologies for the production of solar cells have been extensively researched already for many years, in order to reduce production costs and to increase the conversion efficiency, hence making them even more economically appealing than 1^{st} generation PV. These new (alternative) technologies can be divided in two main categories, depending on their structural characteristics and evelopment phase: 2^{nd} generation (2G) and 3^{rd} generation (3G) technologies.

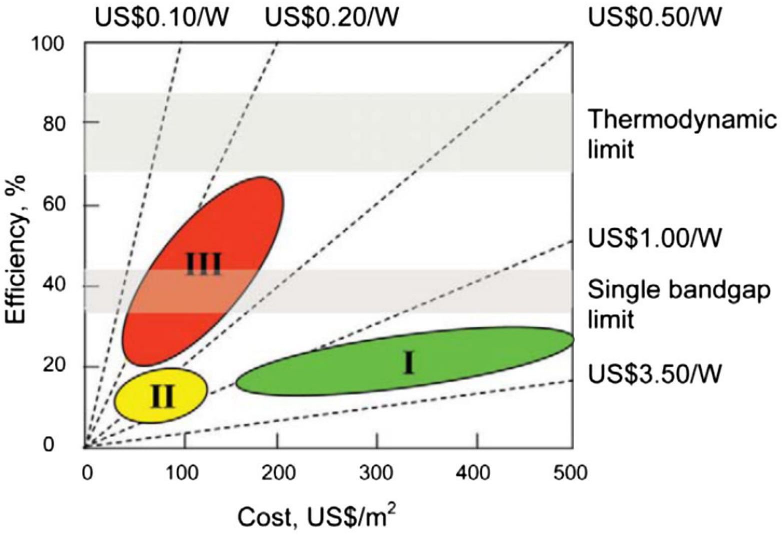

Figure 1-3: Efficiency and cost projections of first- (I), second- (II), and third-generation (III) PV technologies [20].

2^{nd} generation technologies consist of single-junction devices that aim to reduce the material utilization, while maintaining the efficiencies of 1^{st} generation PV [17]. While the absorber layers of wafer-based silicon solar cells consists of several hundreds of μm of material, these 2G solar cells are made of very thin layers deposited on (relatively) inexpensive substrates, like glass, polymer, or metal [17, 21]. As a consequence, a lot less semiconductor material is required to build a cell of the same area, thus production costs can be greatly reduced. On the other hand, such thin absorber layers require the implementation of light-trapping techniques, in order to absorb a sufficient amount of light and thus achieve (relatively) high conversion efficiencies (see Chapter 2).

The primary types of thin-film (TF) single-junction solar cells that have been commercially developed are: amorphous (a-Si) and micro-crystalline silicon (μc-Si), cadmium-telluride (CdTe), Copper-Indium-Selenide (CIS) and Copper-Indium-Gallium-diSelenide (CIGS) solar cells [17, 21].

Thin-film silicon Presently, a-Si and μc-Si cells are, alongside CdTe PV, the most developed and widely known thin-film solar cells [21]. The relatively inexpensive deposition techniques available, combined with the much lower material utilization, makes these type of cells considerably cheaper than their wafer-based counterpart (in terms of specific costs per unit area) [20]. On the other hand, efficiencies are still much lower when compared with 1^{st} generation PV: where current world record conversion efficiencies for wafer-based silicon solar cells are well above 20%, in the case of TF silicon cells these records are 10.1% and 10.8%, for a-Si and μc-Si respectively [22]. The main disadvantage of this type of solar cells is that they suffer from a significant reduction in power output during they lifetime as the sun degrades their performance [21], making thus their stabilized efficiency of such devices significantly lower than their corresponding initial efficiencies [23].

CdTe Cadmium-telluride thin-film solar cells can achieve higher efficiencies then amorphous and micro-crystalline silicon devices, with a current record of 19.6% [22]. The combination of good performance with low production costs makes CdTe the most economical thin-film currently available. The main drawbacks of this technology are related to the absorber materials: availability of tellurium can become a problem, while cadmium has issues concerning its toxicity that may limit its use [21].

CIS and CIGS These types of cells, whose absorber layer is made by a combination of copper, indium, selenium, and eventually gallium, offer the highest conversion efficiencies of all thin-film PV technologies, reaching values as high as 20.8%. The main goals for this technology is now to increase the performance of commercial modules, which is still significantly lower (record efficiency of 15.7%), and to increase the production capacity and reducing its cost [21, 22].

1-2-2 3^{rd} generation PV

3^{rd} generation PV technologies have the goal of increasing the conversion efficiency of previous-generation concepts, while maintaining the same production costs; in this way, it is possible to reduce the final cost of electricity generated [17]. However, it should be noted that most of these technologies are yet to enter the commercial phase, while only a few are beginning to be commercialized [14]. There are numerous 3G technologies currently researched and developed worldwide: from organic solar to dye-sensitized solar cells (DSSC), to multi-junction structures, for both terrestrial and space applications.

Multi-junction approach

This approach consists of using multiple energy levels to absorb different portions of the solar spectrum, reducing in this way the sections which cannot be absorbed by single-junction cells. In order to achieve this, sub-cells made by different materials are stacked on top of each other, from the one with the lowest energy band-gap (bottom cell) to the one with the highest band-gap (on top cell) [20], in this way the top cell can absorb most of the blue spectrum, while the bottom cell operates in the long-wavelength part of the spectrum (see Chapter 2 for further explanation about band-gap energy and related loss mechanisms). The highest quality devices are made by using single-crystal III-V semiconductors (e.g. Gallium-Arsenide, Indium-Phosphide etc.); these cells are usually very expensive to manufacture, due to the non-abundance of such materials and to the high-quality deposition required. For this reason, solar cells made with III-V materials are generally used only in space applications, and usually strong light-concentrators (beyond 500 suns) are implemented, to reduce the cell area and further increase the efficiency [20, 21]. Multi-junction devices can also be realized with silicon thin-film sub-cells, which have the advantage to be much cheaper to manufacture, at the cost of a reduced efficiency. Light-concentration is also possible in this case (although only low- and medium-concentration, up to 100 suns, to avoid overheating), although it is less beneficial in terrestrial applications [20, 21]. Current record efficiencies are over 44% (concentrator) and 38% (non-concentrator) for III-V multi-junction cells (Figure 1-4), and 13.4% for triple-junction silicon cells [22].

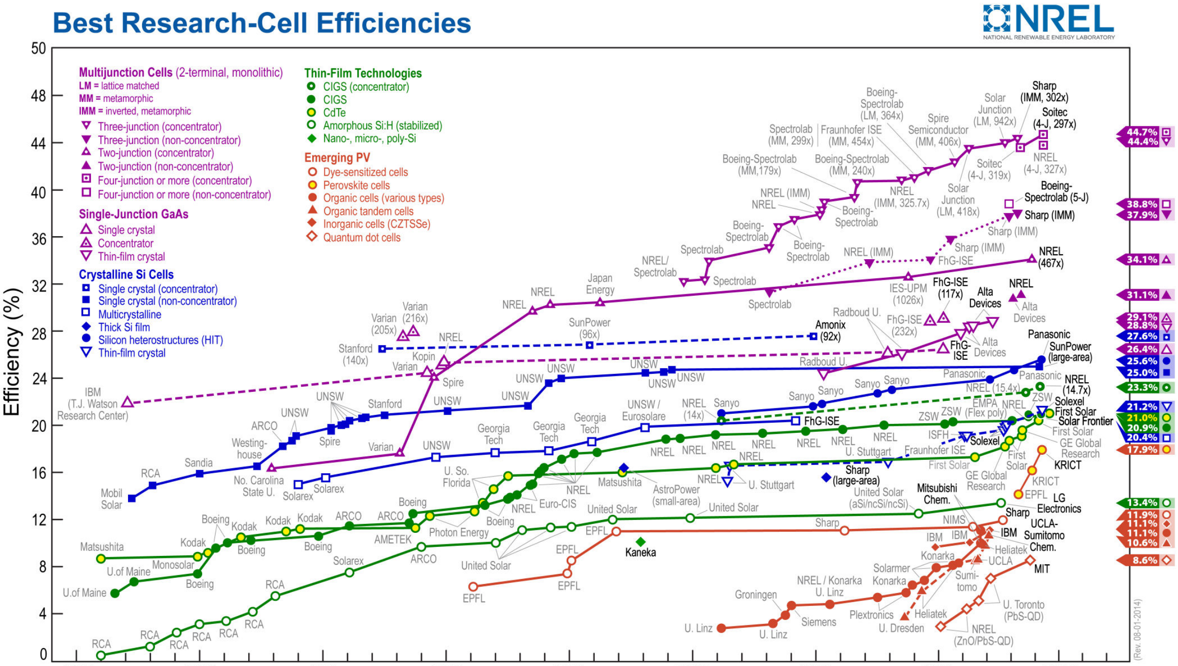

Figure 1-4: Plot of highest confirmed conversion efficiencies for research cells, from 1976 to the present, for a range of photovoltaic technologies [24].

Other approaches

Other 3^{rd} generation technologies have encountered less success, but are still attracting interest due to their potential.

Dye-sensitized solar cells This type of PV cells are based on semiconductor structures formed between a photo-sensitized anode and an electrolyte. In a typical DSSC, the semiconductor nanocrystals harvest the sunlight (photons), and the dye molecule is responsible for the charge separation. These cells are attractive because they use relatively cheap materials and they are simple to manufacture, on the other hand, their performance degrades over time (with exposure to UV light) and they may encounter problems at very low temperatures. Current record efficiencies are relatively low [21].

Organic solar cells These cells are composed of organic or polymer materials. They have the advantage of being inexpensive, but they suffer from low conversion efficiency and instability over time. Despite this, the very low manufacturing costs may allow this type of PV cells to compete with other established technologies in the near future [21, 25].

Novel and emerging concepts In addition to the aforementioned 3G technologies, several other concepts are under development. Among them, the ones attracting more attention are: quantum dots, quantum wells, multiple carrier excitation, up/down conversion and hot carrier cells. Some of these types of solar cells have been already realized on lab-scale, other are still in an early R&D phase, but attention towards them is constantly growing [20, 21].

1-3 Scope & outline of the thesis

The aim of this project can be summarized by the following scientific question:

How does advance texturization of thin-film solar cells influence their optical behaviour and how can such textures be optimized in order to achieve the best possible optical performance?

In the process of answering this question, the following sub-question will be also addressed:

1. How can materials for PV applications be properly characterized?
2. Which are the optimal parameters of 1-D asymmetric gratings for different thin-film technologies?
3. How do material properties affect the optical performance of thin-film silicon solar cells?
4. How do elongated nano-structures affect light propagation inside thin-film silicon solar cells?

These four sub-questions represent the logical order in which the work of this project was carried out: the first step consisted of material characterization, a necessary step to obtain reliable input parameters for the following steps. The rest of the work consisted of optical simulations: first the optimal geometrical properties of 1-D gratings for different TF technologies were found; then the influence of different materials on the optical performance of thin-film silicon cells was studied, identifying which of these materials perform better; finally, the effect of elongated nano-structures on light propagation and optical performance for silicon PV cells was researched, eventually determining the optimal design of such advanced structures.

This final report is structured at follows: after the introduction (Chapter 1), in Chapter 2 the concept of light management is introduced, with an overview of the most important techniques adopted in state-of-the-art solar cells; particular attention is given to those techniques that are analysed in this thesis project, such as textured interfaces and nanowires, presenting in this way the theoretical background of this thesis. In Chapter 3 the equipment used in the optical characterization phase of the project is described, with brief explanations of the working principle of each machine and of the models employed for fitting the experimental data; the results of the material characterization carried out are also presented, providing in this way the answer to sub-question 1. Chapter 4 contains general aspects of 3-D modelling of solar cells and a short description of the software used for the simulations. This provides the background for the following Chapter 5 and Chapter 6, where the results of simulations are summarized, for 1-D gratings and NWs respectively; the analysis of these results give the answer to sub-questions 2, 3, and 4, satisfying the scientific purpose of this work. Finally, Chapter 7 contains the conclusions and an outlook on future work related to the topic of this thesis.

Chapter 2

Light Management in thin-film solar cells

In this chapter the concept of light management is introduced and explained, with the goal to provide a theoretical background to the work of this report. First, the meaning of the term light management is clarified and its importance for thin-film solar cells is explained (Section 2-1). Then, an overview the main loss mechanisms of solar cells and the corresponding light management techniques adopted is presented (Section 2-2). In Section 2-3 and Section 2-4 the analysis is focused on those techniques that were investigated during the course of this project: periodic gratings (which are here compared to alternative random textured) and elongated nano-structures.

2-1 Introduction

Light management is the term commonly used to designate all those techniques applied during the realization of solar cells in order to optimize their optical performance. In particular, the aim of light management is the effective use of the energy contained in the solar spectrum, to maximize the absorption inside the active layer(s) of a PV cell and at the same time minimize the (optical) losses. Light management is particularly important for thin-film (TF) solar cells, since their very thin absorber layers suffer from low absorptivity (due to the very low thickness), especially at wavelengths close to and beyond their material band gap. To understand this, it is useful to look into the absorption mechanisms of light (or electromagnetic waves in general) inside a material.

Light absorption inside thin layers

The intensity of light propagating inside a certain material or medium depends on their optical properties; this behaviour is described by Lambert-Beer's law:

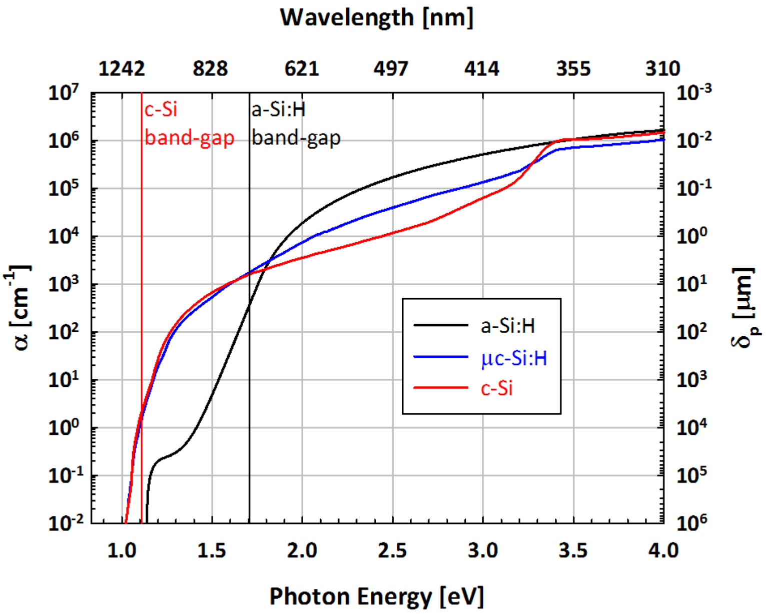

Figure 2-1: Absoprtion coefficients (α, primary vertical axis) and corresponding penetration depths (δ_p, secondary vertical axis) as function of energy (i.e. wavelength), for a-Si:H, μc-Si:H and c-Si [26], with corresponding band gap energies (note that c-Si and μc-Si have the same bangap of $1.11\ \ eV$)

$$I(z, \lambda) = I_0(\lambda) \cdot e^{-\alpha(\lambda)z} \tag{2-1}$$

where $I(z, \lambda)$ represents the intensity of the electromagnetic wave inside the material (as function of the wavelength λ and the path length z), I_0 is the initial intensity (at $z = 0$, at the surface of the material) and $\alpha(\lambda)$ the absorption coefficient of the material, which strongly depends on the wavelength of light (see Figure 2-1). From Eq. (2-1) it is clear that the intensity of an electromagnetic wave propagating inside a material decays exponentially as the travelled distance increase, and this decay gets quicker as the absorption coefficient becomes bigger. A greater intensity decay (α large) implies strong absorption inside the material, while a lower one (α small) allow a bigger portion of light to be transmitted at the back side of the layer (if the thickness z is sufficiently small).

The (wavelength-depending) absorption coefficient $\alpha(\lambda)$ is a property of a material, which can be easily calculated knowing the value of its (complex) refractive index[1] $\tilde{n}(\lambda)$:

$$\alpha(\lambda) = \frac{4\pi}{\lambda}\kappa(\lambda) \ \ [m^{-1}] \tag{2-2}$$

An equivalent way of approaching this problem consists of considering another quantity, specifically the penetration depth ($\delta_p(\lambda)$), instead of the absorption coefficient. The penetration depth measures how deep can a electromagnetic radiation penetrate inside a material,

---

[1] The complex refractive index is expressed by the formula:
$\tilde{n}(\lambda) = n(\lambda) + i\kappa(\lambda)$
where $n(\lambda)$ is the quantity commonly referred to as *refractive index*, while $\kappa(\lambda)$ is the *extinction coefficient*.

and it is defined as the depth at which intensity of the radiation inside the material falls to $1/e$ (approximately 37%) of its original value. Lambert-Beer's law can thus be re-written as follows:

$$I(z,\lambda) = I_0(\lambda) \cdot e^{-\frac{z}{\delta_p}} \tag{2-3}$$

It is indeed possible to see that when $z = \delta_p$, the ratio between light intensity to its initial value is $1/e$. From this follows:

$$\delta_p(\lambda) = \frac{1}{\alpha(\lambda)} \tag{2-4}$$

δ_p is thus inversely proportional to α. This second approach shows clearly how material properties affect the absorption mechanism: if light can penetrate deep inside the material (δ_p large) absorption is weak (slow intensity decay), while a small penetration depth implies strong light absorption (quick decay of the intensity). In general, δ_p is small at short wavelengths (blue light), and gradually increases till it reaches the material band gap; from this point on, the increase becomes steeper (α reduces quickly), meaning that absorption gets very weak (Figure 2-1).

State-of-the-art thin-film PV cells have absorber layers with very small thicknesses, varying from hundreds of nanometers (amorphous silicon) to a few micrometers (micro-crystalline silicon, CIGS) [27]; on the other hand, at wavelengths around and beyond the band gap, δ_p is much larger (hundreds of micrometers, see Figure 2-1). Hence, TF solar cells are not sufficiently thick to absorb light in the longer-wavelength region of the spectrum, unless special light management techniques are implemented.

2-2 Light management techniques

In order to optimize the utilization of the energy contained in the solar spectrum (which from now on will be indicated with AM1.5,see Figure 2-2), the main goal of light management is to reduce the optical losses hindering the cell performance.These loss mechanisms can be divided in three main categories:

- Spectral mismatch
- Front reflectance
- Parasitic absorption in supporting layers[2]

In the following, each of the losses will be discussed and the light management techniques adopted to reduce them will be presented.

---

[2] All the layers of a PV cell that do not contribute to the energy conversion are considered *supporting layers*. Examples are the glass substrate, front and back transparent conducting oxide (TCO) layers and metal contacts/reflectors.

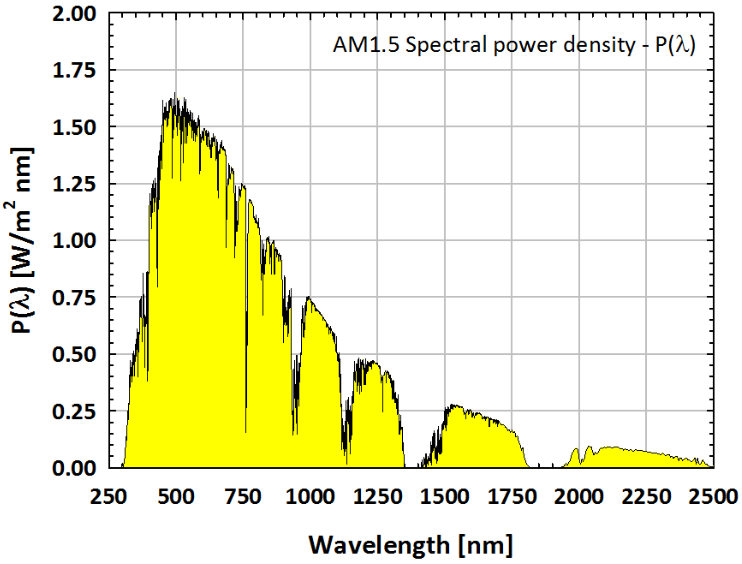

Figure 2-2: AM1.5 spectral irradiance [28].

2-2-1 Spectral mismatch

The term spectral mismatch refers to the mismatch of the photon energy distribution in the solar spectrum and the band gap of the semiconductor material used as absorber layer inside the solar cell. The mismatch results in two intrinsic (unavoidable) losses that reduce strongly the global conversion efficiency of the PV cell. The first one is the non-absorption of photons with energy lower than the absorber material band gap ($E_{ph} < E_g$). These photons cannot excite electrons from the valence to the conduction band (i.e. they are not absorbed) and thus they do not contribute to the energy conversion process [29]. The second loss is the *thermalization*. This process regards the absorption of photons which have a higher energy content than the absorber band gap. The extra energy these photons carry cannot be used to further excite electrons and is thus released as heat inside the material [30]. In Figure 2-3a an example of the mismatch between the spectral power density $P(\lambda)$ and a-Si:H semiconductor between 300 nm and 1200 nm is shown, in this range, almost 13% of the energy is lost for thermalization ($E_{ph} > E_{bg}$), while more than 44% is lost due to non-absorption ($E_{ph} < E_{bg}$).

The standard approach used to reduce the impact of this losses and improve the solar spectrum utilization are multi-junction structures (also known as tandem structures).

Multi-junction structures

Multi-junction structures have been developed already for many years, mainly for cells based on III-V materials for space satellites as well as for thin-film cells based on silicon absorbers [17, 20]; current conversion efficiency world record (considering all technologies, without light concentrators) is hold by a 5 junction cell based on gallium-arsenide (GaAs) and indium-phosphide (InP) absorbers, while double- and triple-junction cells based on amorphous and

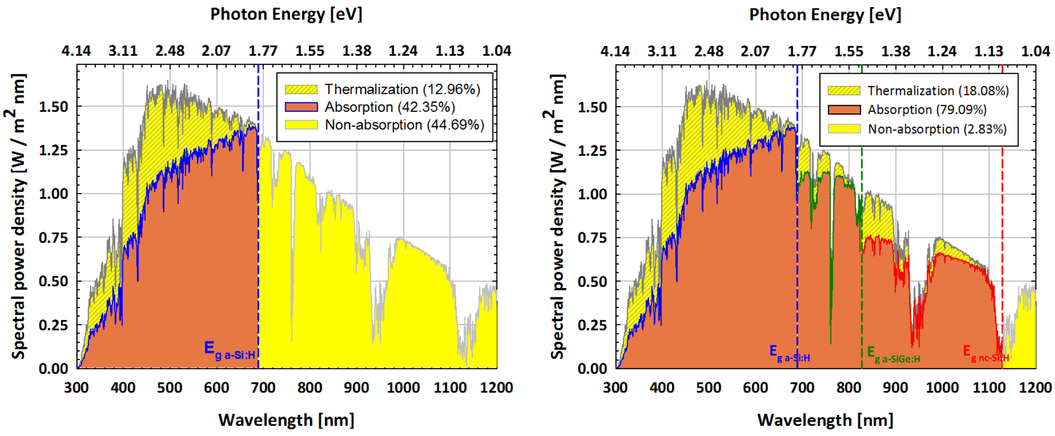

(a) **(b)**

Figure 2-3: Spectral mismatch between spectral power density and an a-Si:H cell (a) and a triple-junction a-Si:H/a-SiGe:H/nc-Si:H (b) [31].

nano-crystalline silicon have already achieved better performance than corresponding single-junction technologies [22, 24].

Multi-junction structures consist of two [32, 33] or more [34, 35, 36] individual cells stacked on top of each other. The sub-cells have absorber materials with different band gaps, going from the largest (top cell) to the smallest (bottom cell); in this way every cell absorbs a specific part of the spectrum: short-wavelength region (blue light) for the top cell, long-wavelength part of the spectrum (red and near infra-red light) for the bottom cell. It is immediately clear that, by sub-dividing the single absorption region of single junction PV cells into multiple regions, the mismatch between the AM1.5 spectral power density and the band gap of the absorber(s) greatly reduces. In Figure 2-3b an example of the mismatch between the spectral power density and a triple-junction cell made of a-Si:H/a-SiGe:H/nc-Si:H is reported, showing how the total losses induced with respect to the single-junction case are reduced (despite an increase of thermalization losses is observed).

While in the case of single-junctions light management is oriented on increasing the value of the short-circuit current density J_{sc}, when dealing with multi-junctions the focus is put on tuning both J_{sc} and V_{oc} (the open-circuit voltage). In fact for single-junction solar cells, once chosen the absorber material, ideally fixing the V_{oc} [37], light managements aims to increase the absorption (i.e. the J_{sc}) as much as possible. In multi-junction structures instead, since the sub-cells are connected in series, the single open-circuit voltages add up, while the short-circuit current density must be equally distributed between the junctions, to achieve current matching [31]. Current matching between the sub-cells is very important, since the J_{sc} of the entire multi-junction cell is limited by the smallest current of its sub-cells (since hey are series-connected).

To achieve optimal current matching the primary approach is tuning the thicknesses of each sub-cell (in particular top cells), in order to make each of them absorbing the right amount of light to generate the same J_{sc}. The material choice is also very important, not only to achieve the highest possible V_{oc}, but also to make each sub-cell absorb only a certain portion of the solar spectrum. For example, if a material with a too low band gap energy were chosen for the top cell, it would generate a higher current density, but bottom cells would absorb less light and thus generate lower currents, reducing in this way the performance of the multi-junction.

An advanced approach to improve current matching and increase the efficiency of multi-junction solar cell is the implementation of intermediate reflectors [31]. Such layers act as optical filters, allowing part of the light (e.g. long wavelengths) to go through to bottom cells and reflecting back to top cell(s) the remaining part of light (short wavelengths). In this way it is possible to keep the thickness of top layers as thin as possible, reducing in this way their light induced degradation. These intermediate reflectors should have low refractive index and low absorption at long wavelengths, in order to allow them to go through to bottom layers; ZnO is a material which fist these requirements and its application as intermediate reflector inside tandem cells has been investigated [38]. Intermediate reflectors based on periodic structures are also under development; distributed Bragg reflectors are notable examples [39, 40].

Other advanced and novel approaches are under investigation for reducing the spectral mismatch between the solar spectral power density and absorber material band-gap(s): among them notable examples are spectrum splitting on laterally dislocated cells [41, 42], up- and down-converters [43, 44, 45] and absorbers with quantum dot super-lattices [31, 46, 47].

2-2-2 Front (primary) reflectance

The primary reflectance, originated by the refractive index mismatch between incident medium (air) and irradiated device, can be reduced by using two different techniques: anti-reflective coating (ARC) and textured front surfaces.

Anti-reflective coatings

An anti-reflective coating consists of one or more layers applied between the absorber and the incident media. Two different concepts are applied: refractive index (step-wise) grading, with the application of the so-called *Rayleigh film* and thickness tuning to achieve destructive interference.

The Rayleigh film is an anti-reflective coating, which is applied to a wide range of technologies, including solar PV cells. The basic concept of a Rayleigh film is interposing between 2 layers a third with a value of the refractive index (n_{ARC}) in between the values of the other two layers (n_0, n_1); in this way primary reflection can be reduced. Any value of $n_0 < n_{ARC} < n_1$ reduces the total reflection, but an optimal value can be found at it corresponds to the geometric average between the indexes of the two neighbouring media [48].

$$n_{ARC}^{opt} = \sqrt{n_0 n_1} \tag{2-5}$$

In Figure 2-4 the effect of the ARC refractive index on an air-glass interface is shown. For this specific materials, n_{ARC}^{opt} is:

$$n_{ARC}^{opt} = \sqrt{n_{air} n_{glass}} = \sqrt{1.5} = 1.22 \tag{2-6}$$

The second parameter of anti-reflective coating which can be tuned is their thickness.The optimal thickness of an ARC layer is:

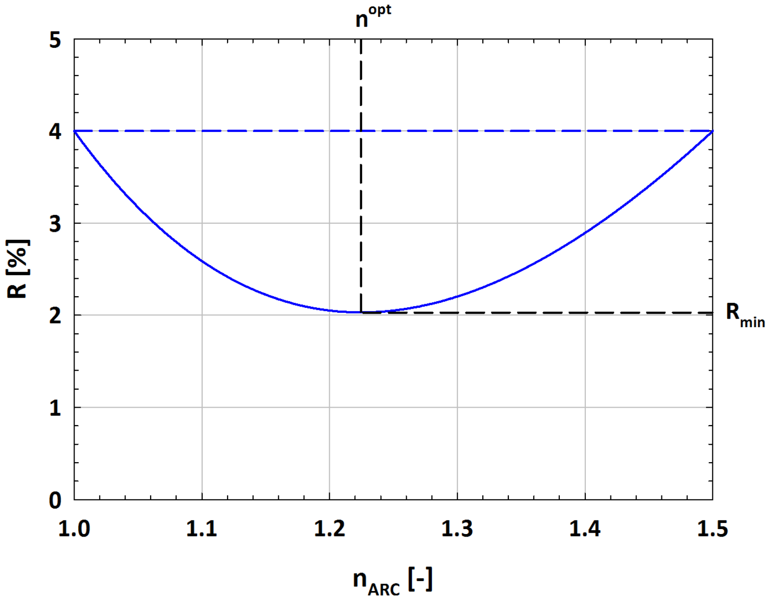

Figure 2-4: Value of the reflectance R for an air-glass interface ($n_{air} = 1$, $n_{glass} \approx 1.5$), with and without an ARC. The optimal value found is: $n^{opt} = 1.22$, which corresponds to a reflectance $R_{min} = 2.03\%$, almost half of the reflectance without ARC (4%).

$$d^{opt}_{ARC} = \frac{\lambda}{4} = \frac{\lambda_0}{4n_{ARC}} \tag{2-7}$$

where λ is the wavelength of light inside the ARC material and λ_0 the wavelength in vacuum. Eq. (2-7) can be found by analysing light interference in a thin layer (Fabry-Perot interference), and the optimal ARC thickness results in destructive interference between reflectance at first and second interfaces (e.g. air/ARC and ARC/absorber).

The technique of anti-reflective coating is clearly only indicative, since the optimal refractive index (Eq. (2-6)) may not correspond to any existing material and , depending on the chosen material, a controlled thickness can be difficult to achieve. Moreover, it must be noted that the thickness optimization is done at a particular wavelength, hence its anti-reflective (AR) effect is limited to a narrow region of the spectrum. To widen such effect, the fabrication of a multi-layer ARC could be a possibility.

Currently, ARC layers position depends on the building technology adopted. For example, in case of *pin* the ARC layer is usually magnesium-fluoride deposited onto the glass superstrate ($n_{MgFl_2} = 1.38$) [49], or titanium-oxide ($n_{TiO_2} = 3$) placed between the front TCO and the p-layer [31, 50]. In the case of an *nip* structure, the various materials used as front TCO (e.g. AZO, ITO) have a refractive index close to the optimal value [51] and their thickness can be tuned to meet both conductance and AR requirements [31].

Textured front surface

The utilization of nano-textures in thin-film silicon PV cells is also very appealing. In fact, the presence of an appropriate front texturization assures a broad wavelength anti-reflection

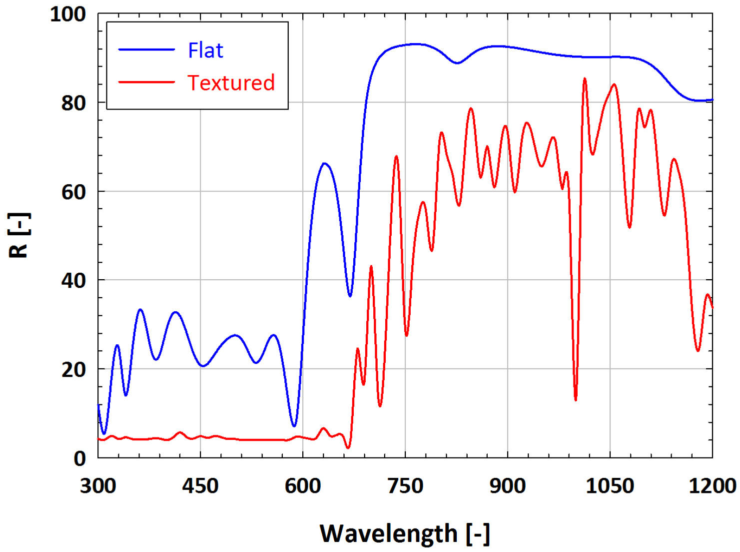

Figure 2-5: Reflectance R of two thin-film silicon solar cell, one with flat interfaces, the other with textured interfaces (1-D diffraction gratings), both with an a-Si:H absorber with a thickness of 290 nm.

effect, since at the interface where the texture is located the refractive index smoothly varies between incident and irradiated media (opposed to the step-wise variation when employing multiple ARC). Texturization is usually applied at the air/device interface, but it is also possible at internal interfaces, promoting a refractive index grading between different layers and thus reducing intermediate reflection [31]. In Figure 2-5 the difference in reflectance between a flat and a textured thin-film amorphous silicon cell is represented, showing the gain achieved with the textured surface.

Front texturization triggers also the scattering of light, but this aspect will be discussed in Section 2-3.

2-2-3 Parasitic absorption in supporting layers

Light which is absorbed by supporting layers in principle does not contribute to the energy conversion process, thus it is considered an optical loss. Recently, a lot of effort has been put into developing transparent conductive oxides (TCO) with low absorption coefficient in the wavelength region of interest ($300 - 1200\,nm$ for Si absorbers) [52, 53]. A growing attention is also given to the development of wide band gap doped semiconductors, such as hydrogenated amorphous/micro-crystalline silicon oxide (a-SiO:H/μc-SiO:H), and to finding alternatives to metallic back reflectors, to avoid parasitic plasmonic absorption on the textured metal surface [31].

2-3 Scattering of light at textured interfaces

Scattering is the phenomenon in which a light ray is deflected from its path due to an impact with a small object. More specifically, textured interfaces with features of micro- and

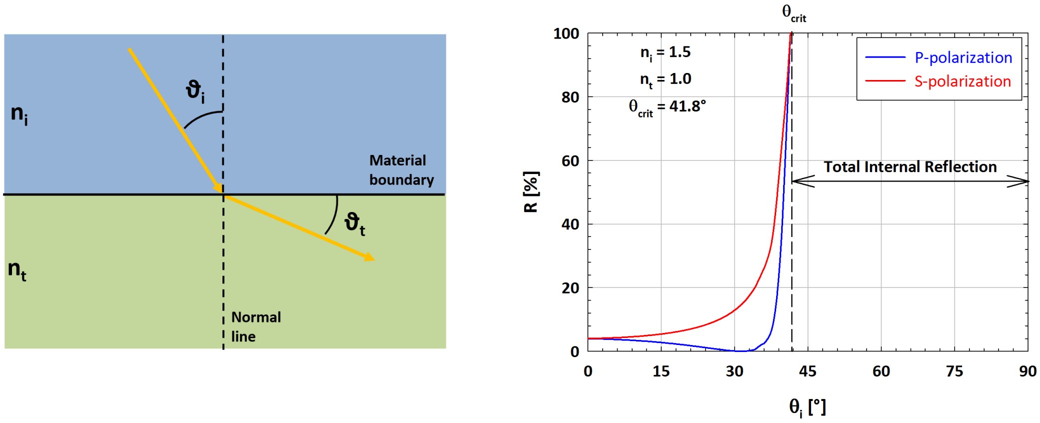

(a) **(b)**

Figure 2-6: Refraction of light when $n_t > n_i$ (a) and value of reflectance R as function of the incident angle ϑ_i, highlighting the limit value of the critical angle ϑ_{crit} (b).

nanometers scale can scatter light, splitting incident perpendicular light rays into multiple rays with directions different from the normal.

Through light scattering it is possible to achieve light trapping, which is the mechanism for which photons are led into the absorber layer and, once there, they are trapped inside it until they are absorbed. In fact, if light is scattered into sufficiently large angles, the phenomenon of total internal reflection can take place. This can be easily seen when considering Snell's law of refraction:

$$n_i \sin \vartheta_i = n_t \sin \vartheta_t \tag{2-8}$$

where n_i and n_t are the refractive indexes of the incident and transmitting media, as shown in Figure 2-6a, ϑ_i is the incident angle and ϑ_t is the transmitted angle. From Eq. (2-8) follows:

$$\sin \vartheta_t = \frac{n_i}{n_t} \sin \vartheta_i \tag{2-9}$$

Considering Eq. (2-9), it is obvious that $n_i > n_t \;\Rightarrow\; \vartheta_t > \vartheta_i$. But if the quantity $\frac{n_i}{n_t} \sin \vartheta_i$ on the right side of Eq. (2-9) becomes greater than 1, than the angle ϑ_t becomes imaginary, i.e. all light is reflected back into the incident media. This phenomenon is called *total internal reflection* and the angle:

$$\vartheta_{crit} = \arcsin \frac{n_t}{n_i} \tag{2-10}$$

is the *critical angle*[3] (see Figure 2-6b).

In the case of thin-film silicon solar cells, after scattered light is reflected by the back reflector it reaches the silicon/TCO interface, with $n_{Si} > n_{TCO}$; hence, if light is scattered at sufficiently large angles, it can be trapped inside the silicon layer, increasing its chances of being absorbed.

---

[3] Note that $\vartheta_i = \vartheta_{crit} \;\Rightarrow\; \vartheta_t = \frac{\pi}{2}$.

Even in the case where the scattering angles are not large enough to achieve total internal reflection, light travels a longer distance inside the absorber layer than in a cell with flat interfaces (no scattering), i.e. the optical thickness of the textured interface is larger than the physical thickness.

To summarize, by introducing textured interfaces inside thin-film solar cells is possible to prolong the effective path length of photons inside the absorber layers, eventually achieving total internal reflection between back and front contacts. Currently, state-of-the-art thin-film silicon solar cells light is scattered at rough interfaces introduced by substrate carriers coated with a randomly surface-textured TCO [31]. However, in recent year the approach of periodic gratings has emerged as a valid alternative. In the following paragraph, the advantages and drawbacks of both possibilities will be examined.

2-3-1 Random textures and periodic gratings

State-of-the-art thin-film silicon solar cells currently employ random textures, which have shown to have outstanding light-trapping capabilities and are relatively easy to manufacture [54]. Over the last years though, the question whether random or periodic periodic nanostructures can lead to better light trapping in solar cells has been hotly debated and remains controversial [55, 56, 57].

The main difference between random textures and periodic gratings lays in the way they scatter incident light. Randomly textured surfaces scatter light into a continuous distribution of angles, allowing the coupling of light to all guided modes but also to the continuum of radiation modes [54]. For a random structure which fully randomizes the incoming light, theory predicts a maximum absorption enhancement of $4n^2$ (where n is the refractive index of the absorber material); this is the famous Yablonovitch limit [58]. On the other hand, periodic gratings scatter light into a discrete set of angles, exciting in this way a finite number of guided modes inside the absorber; the more modes are excited, the higher the absorption becomes. By avoiding the undesirable coupling of light to the continuum of radiation modes, periodic gratings can exceed the Yablonovitch absorption limit, although only in limited portions of the spectrum) [54, 59, 60, 61, 62].

Despite the potential advantage, periodically textured thin-film solar cells have yet to outperform their randomly textured counterparts, mainly because the optimization of the optical performance of periodic gratings (which privileges high aspect-ratio structures) leads to a decrease in the electrical performance, and a trade-off must be found. Recent studies have shown that, by appropriately tuning the grating parameters, periodic structures can perform at the same efficiency levels as their random counterparts. However, further efficiency improvements may only be achieved by designing scalable morphologies which improve the optical performance via higher aspect ratios but avoid an increase of electrical losses [54].

The work of this thesis and the results presented in Chapter 5, rather than discussing the benefits and drawback of periodic textures over random interfaces, will focus on the optimization of 1-D periodic gratings for different thin-film solar cells, analyzing their optical behaviour and absorption enhancement over non textured devices.

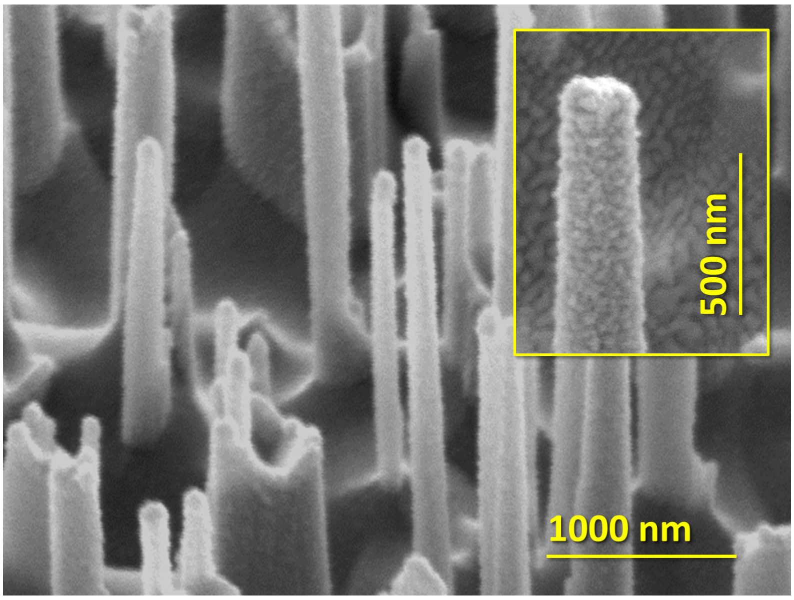

Figure 2-7: scanning electro microscope (SEM) image of a nanowire silicon solar cell.

2-4 Elongated nano-structures for PV applications

Elongated nano-structures, also indicated with the term nanowires (NWs), are promising for the development of advanced light trapping schemes in photovoltaic cells. The term *elongated nano-structures* indicates features of nanometers/micrometers scale which are characterized by very high aspect ratios (i.e. their height is much larger than their cross-section dimension) and that are ideally disposed in a periodic array. There are mainly two types of solar cells based on NWs that can be realized, depending on the type of junction employed: radial junctions or axial junctions. A radial junctions is made of layers deposited on top and around nanowires, which can be metallic, made of TCO or other absorber materials. In this way, the junction is not perpendicular to light illumination as in the case of traditional thin-film cells, but it is radially distributed around the nanowire itself, as in Figure 2-8. On the other hand, in an axial junction the doped and absorber layers are deposited on top of each other to form the nanowires, which are subsequently coated. When comparing these two approaches, the main advantage of the radial junction emerges: the orthogonalization of light travel path with respect to the direction of the charge carrier collection (Figure 2-8a) [63, 64, 65]. The other important benefits of NWs (common to both types of junction) are light scattering from an individual NW to its neighbours, individual reflections between single NWs (Figure 2-8b) and the anti-reflective (AR) effect generated by the particularly high aspect ratio of such elongated nano-structures [63].

Depending on the type of absorber material and junction, several types of NW-based cells can be realized: of those, silicon (Si) radial-junction NWs are the most extensively investigated [64, 65, 66, 67, 68] and reviewed [69, 70], due to the advantages offered by the radial junction configuration (with respect to axial junctions) and to the vast knowledge in Si processing. Other types of structures have been also researched; among them, the most notable are gallium-arsenide radial junctions [71, 72, 73] and zinc-oxide nanorods [74, 75]. In spite of having less advantages than their radial counterparts, axial junctions have also been studied,

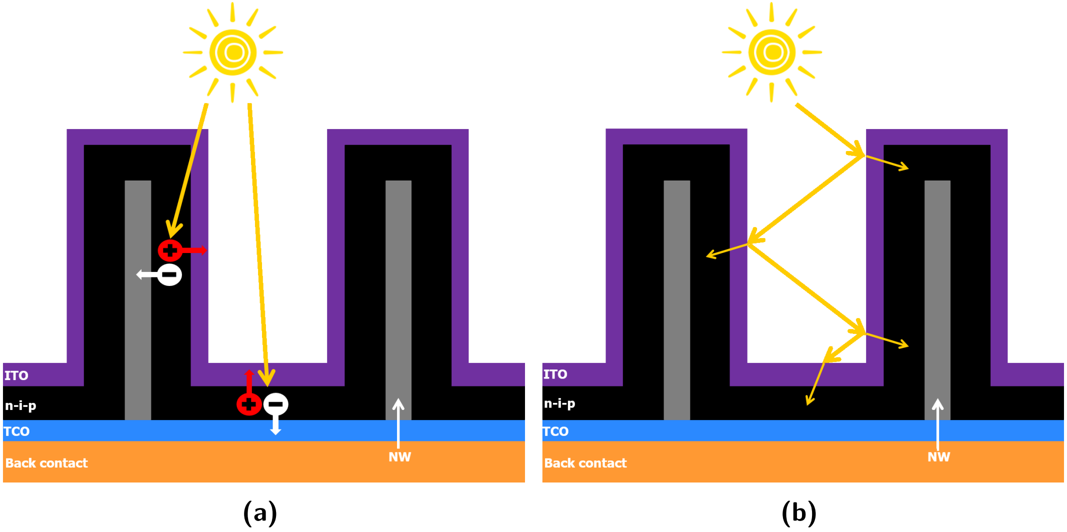

Figure 2-8: Cross-sections of a radial-junction nanowire silicon cell, highlighting the orthogonalization of light and carrier path (a) and multiple reflections between NWs (b).

mostly for structures based on silicon [76, 77]and on III-V absorber materials [78]. III-V materials have the advantage of a longer diffusion length, thus they are more suitable for the axial junction configuration.

In spite of all the research that has been carried out so far, current nanowire-based solar cells developed have shown performance far below equivalent textured thin-film PV cells.The main problem encountered is the inhomogeneous depositions of layers on top of nanowires, which results in a huge reduction of the electrical performance (in terms of V_{oc} and fill-factor FF). Moreover, very small simulation work to optimize the elongated nano-structures, with the exception of the work of Demésy and John [79]. The work and results presented in Chapter 6 are thus of great interest to comprehend how nanowires influence the propagation of light and the performance of thin-film silicon solar cells.

Chapter 3

Optical characterization of materials for PV applications

This chapter provides an overview of the laboratory equipment utilized and the methods employed in order to optically characterize materials for photovoltaic applications (Section 3-1 and Section 3-2); these optical properties extracted are then presented in Section 3-3 and will later be used as input parameters for the simulations in Chapter 5 and Chapter 6.

3-1 Reflectance-Transmittance measurements

Reflectance-transmittance (R-T) measurements were carried out by means of spectrophotometry. This technique allows the measurement of reflectance and transmittance of a sample, with respect to the wavelength of incident light. In a typical spectrophotometer, a source of light impinges on diffraction gratings, which are able to select specific wavelengths of light. Through a series of mirrors the light beam is directed towards the sample. The light transmitted or reflected by the sample is then captured by a detector. Information from the detector is then compared (wavelength by wavelength) to reference transmittance and reflectance spectra, obtaining thus the results in relative terms (i.e. in percentage) [31].

The equipment used to carry out R-T measurements is the Lambda950 by Perkin Elmer (see Figure 3-1). This spectrophotometer is equipped with two light sources, a deuterium arc lamp for ultraviolet light (wavelengths below 320 nm) and a tungsten-halogen lamp, which can cover a wavelength spectrum between up to 3300 nm. Two different accessories can be used with this spectrophotometer: the Integrating Sphere (IS) and the Automated Reflectance/Transmittance Analyzer (ARTA). Both accessories contain two different detectors: a photomultiplier for the ultraviolet (UV) and visible regions of the spectrum and a PbS detector that for the near infrared (NIR) range. The switching between the two detectors takes place at 860.60 nm, which is the weakest operating region for both detectors [80].

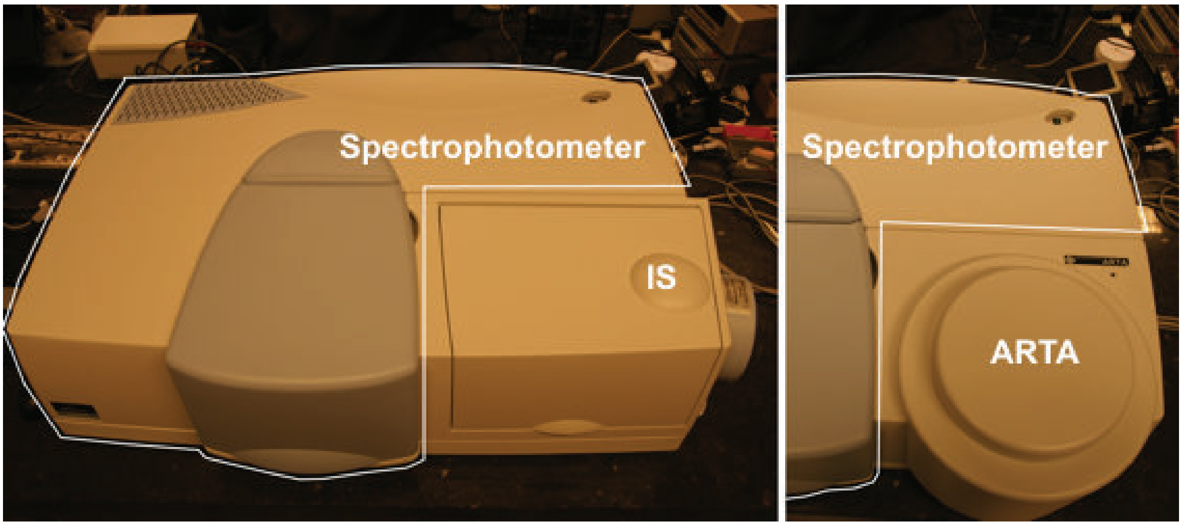

Figure 3-1: The Lambda 950 spectrophotometer by Perkin Elmer, with mounted IS (left) or ARTA (right) accessories [31].

The integrating sphere has a diameter of 150 mm and is internally coated with a highly reflective material with a Lambertian behavior[1]. When light enters through the sample positioned at the transmittance port (see Figure 3-2a), due to multiple internal reflections total (diffuse + specular) transmittance $T_T(\lambda)$ can be measured. In order to measure the diffuse transmittance $T_D(\lambda)$, it is possible to remove a cap located at the reflectance port, opening in this way a hole through which the specular component of transmitted light can leave the sphere. With these measurements, the haze of transmitted light $H_T(\lambda)$ can be easily determined through the following equation:

$$H_T(\lambda) = \frac{T_D(\lambda)}{T_T(\lambda)} \tag{3-1}$$

In a similar way to the transmittance measurements, by positioning the sample at the reflectance port of the IS the total reflectance $R_T(\lambda)$ can be measured as well as its diffuse part $R_D(\lambda)$, once another cap is removed in order to allow the specular component of the reflected light to exit the sphere. In a similar way to H_T, also the haze of reflected light $H_R(\lambda)$ can be calculated by dividing R_D by R_T. Knowing both total transmittance and reflectance, it is also possible to calculate the absorptance of a film ($A_{film} = 1 - R_T - T_T$), in the hypothesis that the substrate carrier on which the layer is deposited does not absorb light in the inspected wavelength range [31].

The ARTA accessory (Figure 3-2b) has a diameter of 180 nm and can be used for two different types of measurements. The first one is the angular intensity distribution (AID) measurement, in which the sample is kept at a fixed angle, while the detector(s) can rotate around it to measure the intensity of transmitted light at different angles. In this way it is possible to determine the intensity of light scattered as function of the scattering angle, which is the

---

[1] A surface which scatters light ideally in all directions is called Lambertian; such surface obeys Lambert's cosine law: $I = k \cdot \cos(\vartheta)$, where I is the intensity of light, k is a proportionality factor and ϑ is the scattering angle.

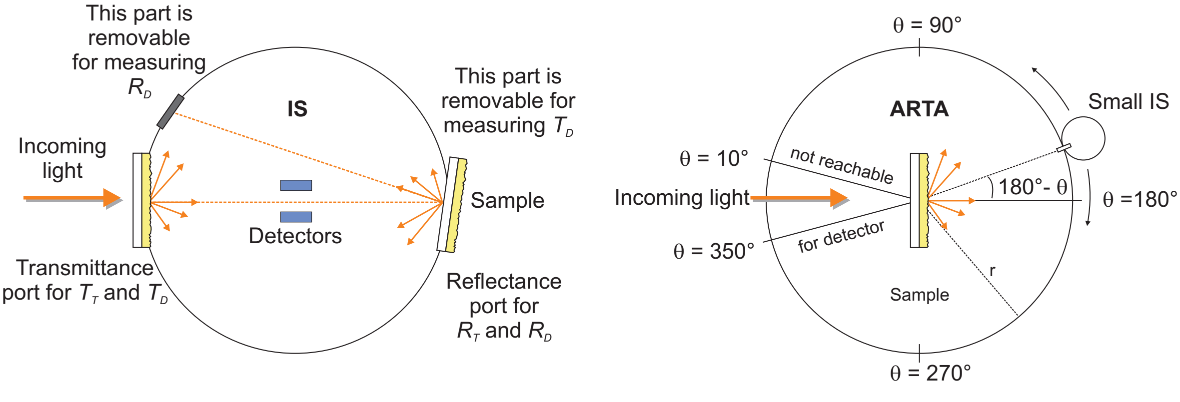

(a) (b)

Figure 3-2: Sketch of the IS (a) and ARTA (b) accessories for the Perkin Elmer Lambda 950 spectrophotometer [31].

AID. These measurements are usually done at one specific wavelength, which must be selected before the beginning of the measurements series. The second type of measurement is the extraction of the n and k values of a material. For this type of measurement, reflectance or transmittance are measured for 17 different positions of sample and detector (see Table 3-1), for both s- and p-polarized light; the total number of measurements for sample is thus 34. For every position, light wavelength is swept between 250 nm and 1500 nm, with steps of 5 nm. The result obtained are then used for the fitting procedure, carried out by the SCOUT software. With this software, the user can create a model that represents the real sample measured with ARTA, which is usually a layer of material deposited on a previously characterized substrate. SCOUT will then iteratively adjust various properties of the layer, among them thickness, band gap energy and roughness, until the model curves fit the corresponding measured ones. When the fit is satisfying (i.e. when the RMS error of the fitted curve is sufficiently small), the fitting process stops and the material is properly characterized, and the value of the complex refractive index $\tilde{n}$ as well as the other aforementioned properties (band gap, thickness etc.) can be exported.

3-2 Spectroscopic ellipsometry

Ellipsometry is an optical technique for investigating the dielectric properties (complex refractive index or dielectric function) of thin films. Ellipsometry can be used to characterize composition, roughness, thickness (depth), and other material properties. It is very sensitive to the change in the optical response of incident radiation that interacts with the material being investigated. The term *spectroscopic* refers to the broad-band light source employed, as opposed to single-wavelength ellipsometry where the light source used is monochromatic.

The parameter measured by the ellipsometer is the change in polarization as the incident radiation interacts with the measured sample. In the most common configuration, light illuminating from an incident angle larger than 0 (perpendicular illumination) is reflected by the sample and the specular component of reflected light is collected by a detector positioned symmetrically to the light source. The polarization change can be quantified by the amplitude

Table 3-1: Position of sample and detector for n, κ extraction with the ARTA accessory.

Position	Sample angle [deg]	Detector angle [deg]
1	-60	240
2	-45	270
3	-30	300
4	-15	330
5	15	30
6	30	60
7	45	90
8	60	120
9	-60	180
10	-45	180
11	-30	180
12	-15	180
13	0	180
14	15	180
15	30	180
16	45	180
17	60	180

ratio, Ψ, and the phase difference, Δ, between incident and reflected light. Ψ and Δ are related by Eq. (3-2):

$$\tan(\Psi) \cdot e^{i\Delta} = \rho = \frac{r_p}{r_s} \tag{3-2}$$

where ρ is defined as the ratio of the reflectivity for p-polarized light (r_p) to the reflectivity for s-polarized light (r_s). The term $\tan(\Psi)$ represents the magnitude of the reflectivity ratio and Δ its phase [81]. Because the reflected signal depends on the thickness as well as the material properties, ellipsometry can be a universal tool [82] for contact free determination of thickness and optical constants of films of all kind.

The equipment that was used for spectroscopic ellipsometry characterization is the ESM-300 spectroscopic ellipsometer by J.A. Woolam Co. (see Figure 3-3). It consists of a light source, which emits a beam of broad-band light towards the sample holder, where the sample is positioned. The robotic arm holding the light source can rotate to change the angle of incidence of light on the material. On the other side of the machine a symmetric arm holds the detectors. The two arms move together in order to to allow the detectors to collect the specular component the light reflected by the sample. There are two detectors present, one for UV and visible light and the other for NIR light. In order to operate the ellipsometer, the CompleteEASE software is required.

The procedure to follow in order to extract the sample properties is the following: first, after calibration, a sample is measured at different angles of incidence. Then, the CompleteEASE software can extract the values of Ψ and Δ as function of the wavelength λ for the angles of incidence measured. After that, the user creates a model that mimics the real structure of

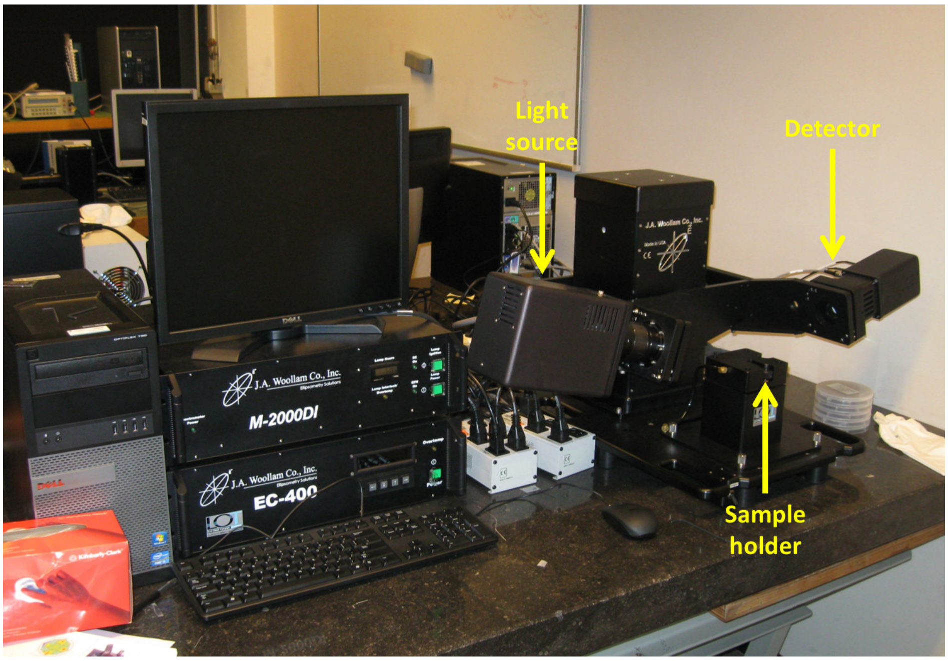

Figure 3-3: The J.A. Woolam Co. ESM-300 spectroscopic ellipsometer.

the device. This is the most delicate part, since depending on the material to characterize different models with different oscillator functions must be used. After a model is chosen, the software starts the fitting procedure, where different parameters of the oscillator functions as well as other parameters of the measured layer, such as thickness and surface roughness, are iteratively adjusted until the modelled functions fit the measured curves. Finally, if the fitting is considered sufficiently accurate, the optical properties of the material as well as the thickness of the layer and the roughness of the surface can be obtained. In particular, the optical property that can be extracted is the complex dielectric function $\tilde{\varepsilon}$. Knowing the relation between $\tilde{\varepsilon}$ and the complex refractive index $\tilde{n}$:

$$\tilde{\varepsilon} = \varepsilon_1 + i\varepsilon_2 = (n + i\kappa)^2 \tag{3-3}$$

It is possible to determine the values of the real part of the refractive index n and the extinction coefficient κ:

$$n = \sqrt{\frac{\sqrt{\varepsilon_1^2 + \varepsilon_2^2} + \varepsilon_1}{2}} \tag{3-4}$$

$$\kappa = \sqrt{\frac{\sqrt{\varepsilon_1^2 + \varepsilon_2^2} - \varepsilon_1}{2}} \tag{3-5}$$

Table 3-2: Samples provided by Forschungszentrum Jülich GmbH (FZJ). (* *For n- and p-doped layers two samples were provided, to allow to allow a more precise characterization.*)

Sample	Nominal thickness [nm]	Measured thickness [nm]
Asahi-U TCO	[not given]	721
ZnO:Al TCO	[not given]	1017
p-doped a-Si:C:H	15/85*	13.7/80.2
n-doped a-Si:H	20/100*	20.3/95
intrinsic a-Si:H	290	258
p-doped μc-Si:H	30/83*	24.4/72.2
n-doped μc-Si:H	32/98*	36.2/96.1
intrinsic μc-Si:H	435	453

3-3 Material characterization results

Two set of samples were characterized in this project: the first, provided by the Forschungszentrum Jülich GmbH (FZJ) [83], consisted of materials that were later used in the modelling of amorphous and micro-crystalline silicon thin-film solar cells: hydrogenated-silicon absorber layers, silicon doped layers and TCO layers (see Table 3-2). The second set of samples, provided by Commissariat á l'Energie Atomique (CEA) [84], consisted of the materials used in the modelling of the CIGS PV cell: molybdenum (Mo) reflector, CIGS absorber, CdS and TCO layers (Table 3-3).

Table 3-3: Samples provided by Commissariat á l'Energie Atomique (CEA).

Sample	Nominal thickness [nm]	Measured thickness [nm]
CIGS	660	671
CdS	50	45
ZnO:Al	400	443
ZnOi	50	49.9
Mo	500	500

3-3-1 Extraction of reflectance and transmittance profiles

For all the samples, spectrophotometry measurements were carried out, using the IS accessory as described in Section 3-1. The results of this measurements consist of reflectance and transmittance profiles (in percentage terms) over the measured spectrum (300-1500 nm). For textured samples, both the total and diffused transmittance were measured, to allow the calculation of the haze parameter $H_T(\lambda)$ with Eq. (3-1). In the case of samples made by FZJ, a comparison between the obtained R,T curves and the corresponding data provided by the manufacturer was done. In Figure 3-4 the curves obtained for one FZJ and one CEA sample are shown.

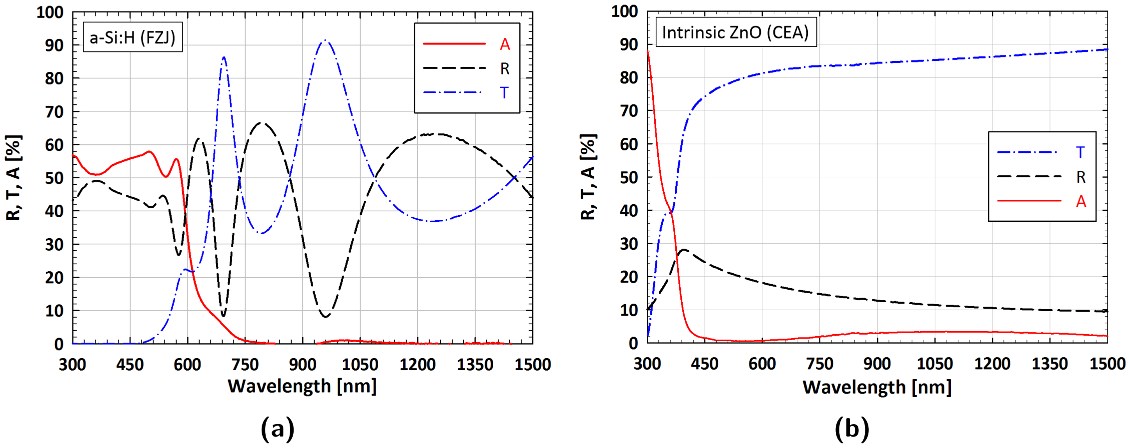

Figure 3-4: Reflectance R, transmittance T and absorptance A ($A = 1 - R - T$) of an a-Si:H sample provided by FZJ(a) and an intrinsic ZnO sample provided by CEA (b)

.

3-3-2 Determination of n, κ data

Regarding the extraction of the n, κ data, a choice had to be made on whether to employ the spectrophotometer equipped with the ARTA accessory or use spectroscopic ellipsometry. Previous works [85, 86] showed that ARTA is preferable for measuring the n, κ values of transparent conducting oxides, especially when the samples measured are not flat (as was the case for the Asahi-U and the etched ZnO:Al samples provided by FZJ). Additionally, the work by Sap et al. [86] proved that the presence of a surface roughness does not prevent the correct determination of complex refractive index values, if such roughness is appropriately included in the fitting model used. For this reason, TCO samples were characterized through spectrophotometry (with ARTA), while all the properties of the remaining samples were determined by spectroscopic ellipsometry.

Extraction of n, κ values of transparent conductive oxide layers

In total 4 TCOs were characterized: 2 of them were provided by FZJ (one Asahi-U sample and one ZnO:Al sample, see Table 3-2) and 2 by CEA (another ZnO:Al sample and an intrinsic ZnO layer, see Table 3-3). The models used for the fitting process in the SCOUT software where previously developed inside the Photovoltaic Materials and Devices (PVMD) group at Delft University of Technology. For all samples the fitting results were sufficiently accurate (final standard deviation below 0.005, which is the same iteration stopping criteria used by Sap et al. in [86]), and the results found good correspondence with values present in literature [86]. The results of the characterization of the four TCOs is presented in Figure 3-5.

Extraction of n, κ values with spectroscopic ellipsometry

Spectroscopic ellipsometry (SE) was used to characterize all the remaining materials (see Table 3-2 and Table 3-3). The CompleteEASE software used for the fitting process contains already built-in models for multiple different materials, which were used in this project when

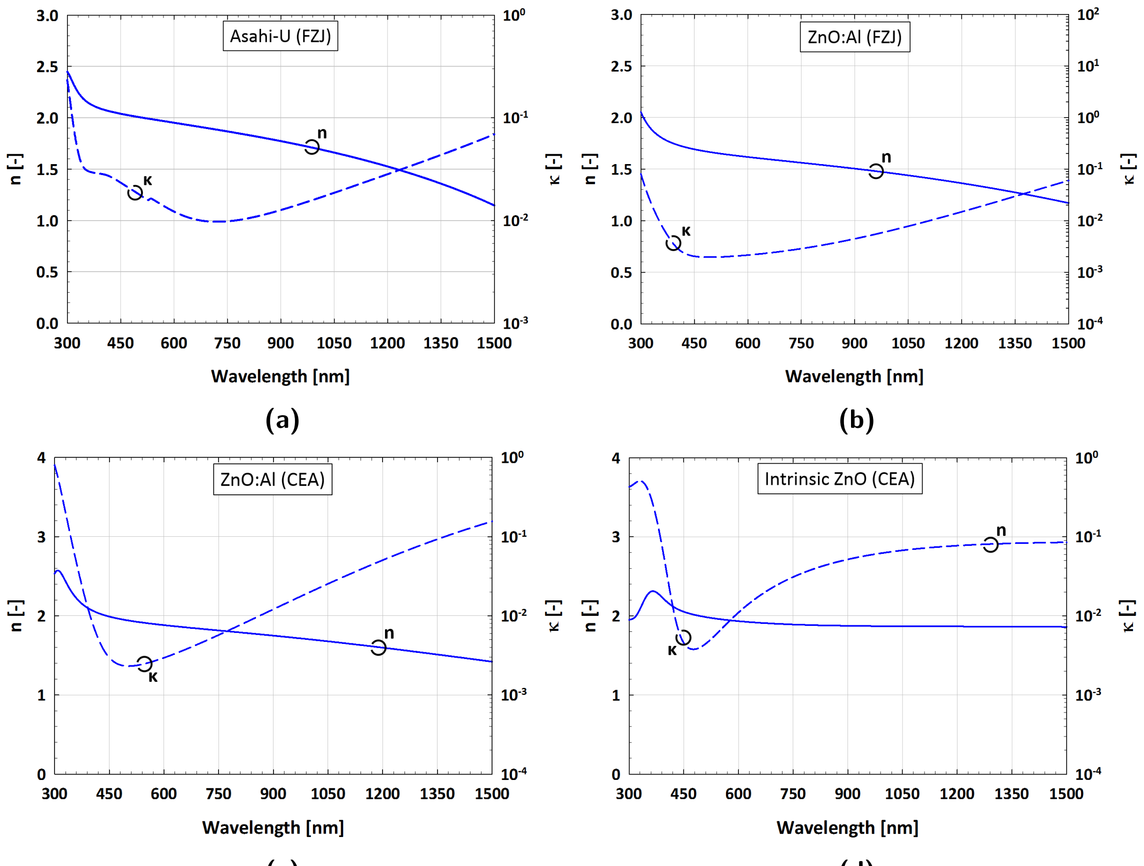

(a) (b)

(c) (d)

Figure 3-5: n, κ profiles of Asahi-U (a), ZnO:Al from FZJ (b), ZnO:Al from CEA (c) and intrinsic ZnO (d)

deemed sufficiently accurate. For the silicon samples, different models developed by the PVMD group were used, since they gave better results than corresponding built-in models.

Particular attention must be put in the characterization of doped layers, presented in Figure 3-6. In fact, these layers show relatively high levels of absorption at wavelengths beyond the material band gap (around 730 nm for a-Si:H and 1100 nm for μc-Si:H), due to the well-known phenomenon of free-carrier absorption [87]. Hence, if the model is not correctly defined, the fitting process will give incorrect results. For this reason, specific models for doped silicon layers were used for the characterization of n- and p-type doped materials. In Figure 3-7 the extracted n, κ values for intrinsic a-Si:H are presented, showing the quick decay in absorption (κ) at the material band gap.

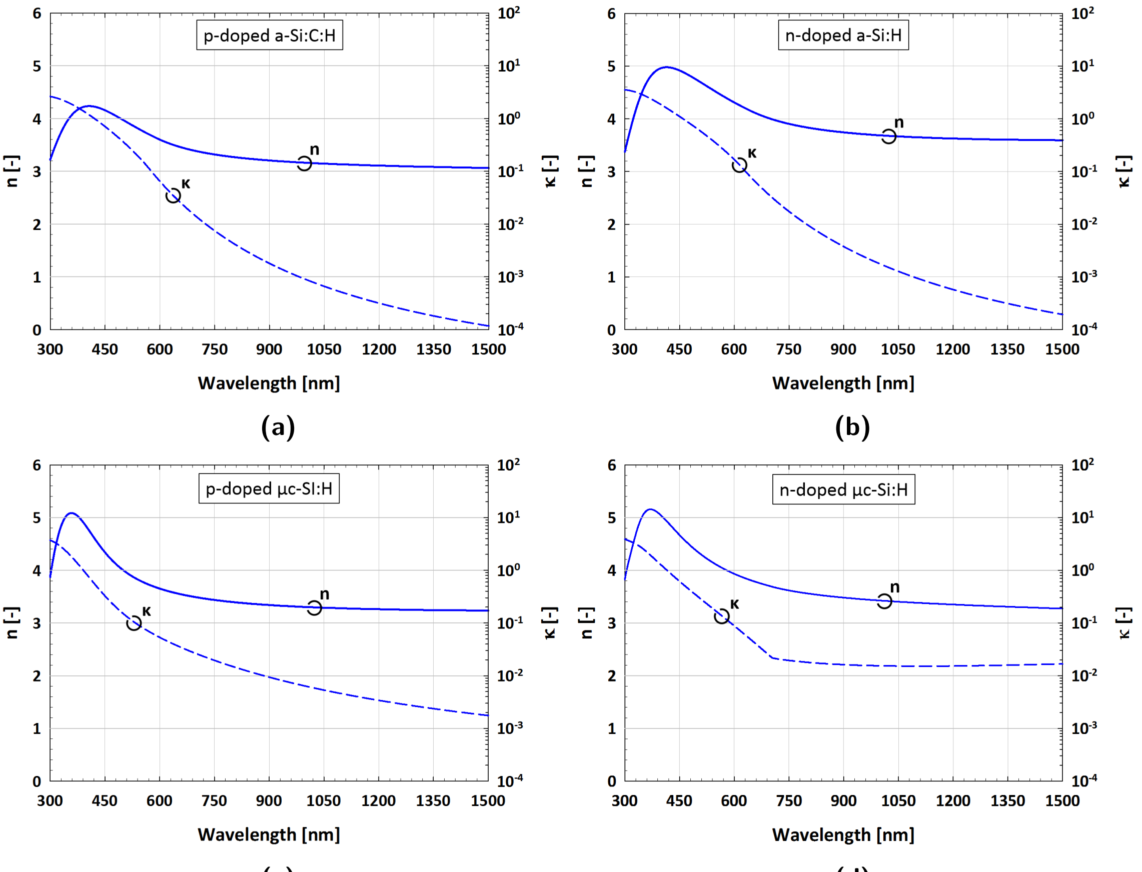

(a)

(b)

(c)

(d)

Figure 3-6: n, κ profiles of p-doped a-Si:C:H (a), n-doped a-Si:H (b), p- (c) and n-doped μc-Si:H (d), which show relatively high values of κ also at long wavelengths due to free-carrier absorption

.

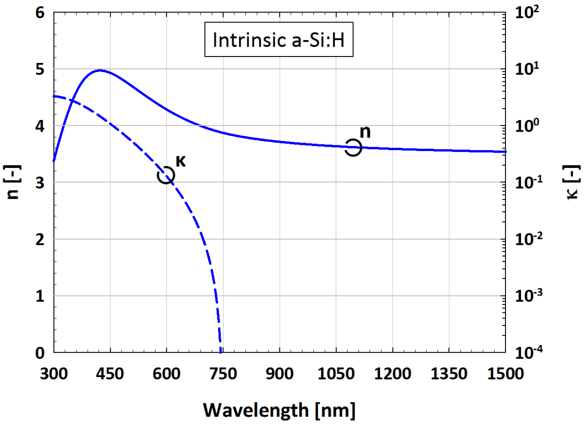

Figure 3-7: n, κ profile of intrinsic a-Si:H; note that κ decreases rapidly when approaching wavelengths close to the material band gap ($\approx 730nm$).

Chapter 4

Solar cell 3-D optical modelling

In this chapter a description of the modelling approach used to carry out the simulation work of this thesis is presented, alongside a brief description of the software employed and the procedure followed.

4-1 The Finite Element Method

The Finite Element Method (FEM) is a numerical technique to find approximate solutions of Maxwell equations. When using FEM, the volume of the simulated structure is meshed (i.e. discretised) with tetrahedrons and the components of the electromagnetic field are calculated at their vertices (nodes) [31]. In this method, the Faraday and Ampere-Maxwell laws are combined to obtain Helmoltz vector equation [88] in terms of the electric field **E** (Eq. (4-1)) or the magnetic field **H**:

$$\nabla \times \frac{1}{\mu_r} \nabla \times \mathbf{E} - k_0^2 \varepsilon_r \mathbf{E} = i k_0 Z_0 \mathbf{J} \tag{4-1}$$

where **J** is the electric current density (in A/m^2), ε_r and μ_r are, respectively, the relative permittivity and magnetic permeability of the medium, $k_0 = 2\pi f \sqrt{\mu_0 \varepsilon_0}$ is the wavenumber in vacuum and $Z_0 = \sqrt{\mu_0/\varepsilon_0} = 377\ \Omega$ is the impedance of free space. Applying different methods, it is possible to combine Eq. (4-1) and its dual equation on the magnetic field into the matricial form $\underline{\mathbf{A}} \cdot \mathbf{x} = \mathbf{b}$. The vector $\mathbf{x}$ contains the unknown (spacial) components of the electromagnetic field, while the vector $\mathbf{b}$ is determined by the boundary conditions and forced excitation (and is thus known). The matrix $\underline{\mathbf{A}}$ is square, sparse and symmetric, and its elements indicate the material properties at the nodes. Such system of equations can be solved by the application of iterative or direct techniques. Direct solving methods are used only for small size problems, since they are computationally very demanding. Hence, typically iterative method-based procedures are used, thanks to their efficient handling of sparse linear systems. FEM can achieve a very accurate modelling of inhomogeneous materials and complex non-conformal geometries, thanks to its flexible meshing capability. These features make FEM the

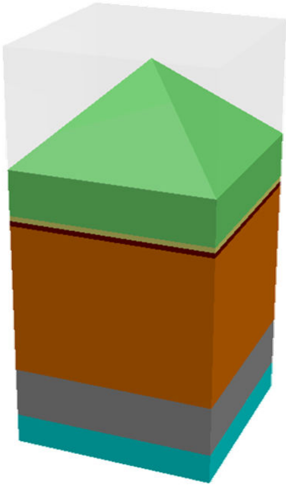

Figure 4-1: Example of a solar cell model, with different layers indicated by different colours.

preferable choice to solve electromagnetic problems over complicated structures, such as the ones created for this project, provided a sufficient amount of random access memory (RAM) is available to create the mesh [31].

4-2 The High Frequency Structure Simulator software

The High Frequency Structure Simulator (HFSS) was the FEM software used in this work. Its algorithm can find solutions for 3-D electromagnetic problems also at optical frequencies. The procedure followed to create and solve the models was:

1. Design of the model
2. Definition of boundary conditions and frequency sweep
3. Solving the electromagnetic problem
4. Exporting solutions

In the following, each of the aforementioned steps will be briefly described.

Model design

HFSS is equipped with a CAD interface that allows the user to easily design complex 3-D geometries. For multi-layer structures, the user must create a geometry for each of the layers, and then combine them to obtain the full structure (see Figure 4-1). The top layer must have a flat surface, to allow the definition of the field excitation. After all the geometry of the model is defined, the user must assign to each layer a material, which properties can be imported from measurements. The materials must be defined by the real part of the dielectric function ε_1 and by $T_{loss} = \varepsilon_2/\varepsilon_1$, the ratio of the imaginary to the real part of the (complex) dielectric function $\tilde{\varepsilon}$. Knowing the value of the (complex) refractive index $\tilde{n}$ and its relation with $\tilde{\varepsilon}$ (Eq. (3-3)), ε_1 and T_{loss} can be determined as follows:

$$\begin{cases} \varepsilon_1 = n^2 - \kappa^2 \\ T_{loss} = \frac{\varepsilon_2}{\varepsilon_1} = \frac{2n\kappa}{n^2-\kappa^2} \end{cases} \tag{4-2}$$

Definition of boundary conditions and frequency sweep

After all layers have a material assigned, the user must define boundary conditions. By setting them up appropriately, large solar cell models can be reduced to small structures, reducing in this way the simulated volume to the so-called unit cell [89]. The unit cell serves as the problem domain for boundary conditions, extending the computational volume in directions x, y and z (see Figure 4-2). The boundary conditions used in the simulations of this work are: (i) the master-slave (M-S) boundary condition [90] acting on the surfaces parallel to te xz- and yz-planes, (ii) the Floquet ports [91] acting of surfaces parallel to the xy-plane and (iii) the Perfect E-Perfect H (PE-PH) symmetry conditions [92].

The M-S is a boundary condition applied to parallel surfaces in order to mimic the periodicity along their normal direction [89]. The components of the electromagnetic field calculated at the *master* surface are equalized to those at the *slave* surface. The components at the *slave* surface can be phase shifted with respect to *master* components; the phase shift Φ is defined as follows:

$$\Phi = \frac{d_{M-S}}{\lambda} sin\theta cos\phi \tag{4-3}$$

where d_{M-S} represents the distance between the two linked boundary surfaces, while θ and ϕ are the polar angles representing the direction of the incident field. In the simulations of this work, Φ has been set in most cases to zero, in order to consider only perpendicular incidence of light.

Floquet ports are adopted at the top horizontal surface of the unit cell, to represent efficient absorbing boundary conditions. FPs simulate infinite media in which light can propagate almost without reflection to the infinity. They have been preferred to alternatives such as perfectly matched layers (PML) because of faster meshing time required and easier determination of front reflectance [89]. FPs could have been used also at the bottom horizontal surface of the unit cell, to measure transmitted light, but the presence of sufficiently thick metal back reflectors at the bottom of the simulated structures unnecessary. To prove it, after every simulation an energy balance was set up, and every time the sum of reflectance R and absorptance in each layer of the structure $\sum A_i$ was equal to 1, proving that no light was in fact transmitted at the back of the simulated structures.

PE-PH conditions allow the user to further reduce the dimensions of the unit cell in case of symmetric structures. In fact, if the original unit cell consists of 1-D or 2-D symmetric gratings, by applying these symmetry conditions the volume can be reduced, respectively, to 1/2 and 1/4 of the original, as shown in Figure 4-2(c) and (d). When applying symmetry conditions to structures with one symmetry plane (e.g. 1-D symmetric gratings), a choice

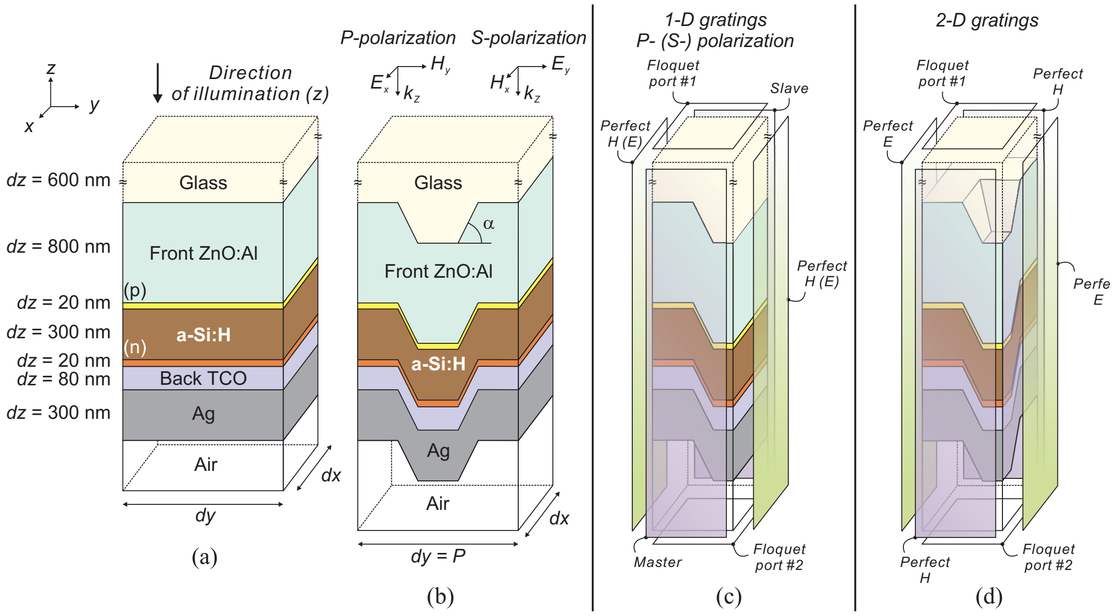

Figure 4-2: Unit cells of thin-film solar cells: flat (a), with 1-D gratings (b), with 1-D gratings and symmetry conditions applied (c) and with 2-D gratings and symmetry conditions applied (d) [89].

must be made on whether to use PE or PH conditions, depending oh which of the vertical planes is the symmetry plane and on how p- and s- polarizations are defined.

Finally, after all boundary conditions have been appropriately imposed, the frequency sweep has to be defined. The user can select the starting and finishing frequency as well as the step size. For the simulations done in this work, a constant wavelength step size was preferable to a constant frequency step size. In order to define and import the frequencies corresponding to a uniform wavelength step size, a simple MatLab code was used, based on the formula that relates the wavelength λ and frequency f:

$$f = \frac{c}{\lambda} \tag{4-4}$$

where c is the speed of light in vacuum ($c \approx 3.0 \times 10^8\ m/s$).

Solving the electromagnetic problem

Once the design of the simulation is set up (structure, material properties, boundary conditions etc.), FEM-based algorithms in HFSS operate through three phases: *meshing*, *solving*, and *sweeping*. First, the volume of the designed structure is discretised in tetrahedrons. Then, the linear system of equations $\underline{\mathbf{A}} \cdot \mathbf{x} = \mathbf{b}$ is iteratively solved; at each iterative step the number of tetrahedrons increases to better approximate the structure (*mesh adaptation*), until convergence is achieved. Finally, the electromagnetic field is calculated for each wavelength previously set up [31]. Parameters such as minimum and maximum number of iterations, convergence tolerance etc. can be defined by the user.

Exporting solutions

Once the algorithm found a solution at all the wavelengths set up, it is possible to extract the solutions. The two parameters of interest for this work are the total reflectance R and the absorptance in individual layers A_i. The total reflectance, which is an output parameter of the simulation, can be calculated in terms of S-parameters [89] as $R = |S_{11}|^2$. The absorbptance of the generic layer i can be calculated by integrating the square magnitude of the electric field E over the volume of the film:

$$A_i = \frac{1}{2}\varepsilon_0 Im(\tilde{\varepsilon_i})\omega \int\limits_{V_i} |E|^2 \, \mathrm{d}V \tag{4-5}$$

where ε_0 is the dielectric constant of vacuum, $\tilde{\varepsilon_i} = \tilde{n}^2$ is the complex relative permittivity of the i-th material ($Im(\tilde{\varepsilon_i}) = \varepsilon_2 = 2n_i\kappa_i$) and ω is the anglular frequency. As stated earlier, the transmittance T was negligible, and thus the energy conservation law can be written as follows:

$$R + \sum A_i = 1 \tag{4-6}$$

By convoluting the absorptance A_i with the reference photon flux $\Phi(\lambda)$ of air mass 1.5 in the considered wavelength range, the (implied) photocurrent density or integrated optical losses generated in the i-th layer (J_{ph-i}) can be calculated as follows [89]:

$$J_{ph-i} = -q \int A_i(\lambda)\Phi(\lambda)\mathrm{d}(\lambda) \tag{4-7}$$

where q is the elementary charge. For the absorber layer, this implied photocurrent density J_{ph} can be a first approximation (which does not take into account electrical loss mechanisms) of the short-circuit current density J_{sc} of the device.

Chapter 5

Optical modelling of 1-D asymmetric periodic gratings for thin-film solar cells

In this chapter, the results of the modelling of 1-D periodic gratings fro thin-film solar cells are given. First the modelling of 1-D asymmetric periodic gratings for PV cells based on an amorphous-silicon-based absorber is presented (Section 5-1). Then, results of simulations for the micro-crystalline silicon thin-film cell are shown (Section 5-2). Finally, the modelling of the CIGS solar cells is presented(Section 5-3). For all the three devices, first the modelled structures are described, then the results are presented and discussed.

5-1 Amorphous silicon thin-film solar cells

A possible way to increase the optical performance of cells with periodic gratings is using asymmetric features in place of the usually employed symmetric structures. For this reason the effect of the asymmetry of gratings has been analysed in this project, for devices based on three different absorber materials: hydrogenated amorphous silicon, micro-crystalline amorphous silicon and CIGS.

Of the three absorber materials investigated, hydrogenated amorphous silicon (a-Si:H) has the highest band gap energy ($E_g \approx 1.7\ eV$, corresponding to $\lambda_g \approx 730\ nm$). Moreover, since the amorphous structure of this material results in a very short minority carrier diffusion length, cells based on a-Si:H must have very thin absorber layers to be able to efficiently collect the generated charges. Hence,thick layers would be necessary to efficiently absorb light, especially in the spectral region close to the material band gap, but from an electrical point of view thin layers are preferable . Currently, state-of-the-art amorphous silicon PV cells have an absorber layer thickness d_{abs} around 300 nm, which represent the balance between carrier diffusion length and optical absorption [27].

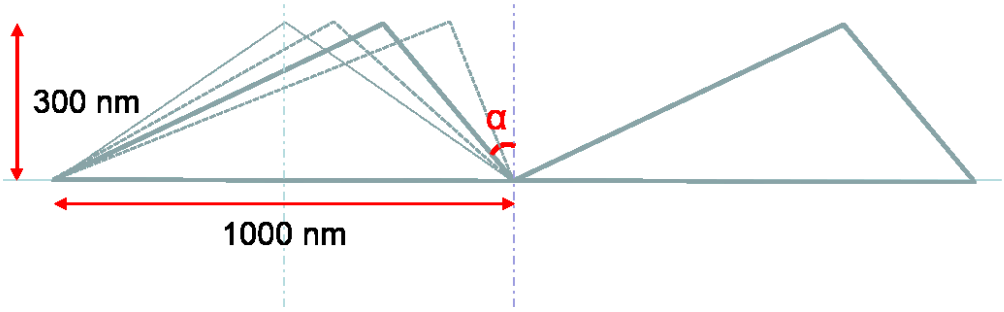

Figure 5-1: Sketch of the a-Si:H-based solar cell triangular grating cross-section, indicating period ($P = 1000\ nm$), height ($h = 300\ nm$) and inclination angle α.

5-1-1 The model

The work done by Isabella et al. [89] showed that the optimal geometric dimensions of periodic gratings for a-Si:H-based thin-film cells are a period P of 1000 nm and a height h of 300 nm. It was thus decided to fix the values of these two parameters, as well as the shape of the gratings (triangular), to focus the analysis only on the asymmetry of the structure. Starting from the symmetric case, the inclination of the sides of the triangle with respect to its base was gradually changed until one of them became vertical (forming an angle of 0° with the normal to the base). In total, 4 different angles were considered (Figure 5-1): 59° (angle of the symmetric isosceles triangle),40°, 21°, and 2° (vertical case[1]).

Table 5-1: Structure, materials and relative thicknesses of the a-Si:H solar cell model using traditional materials.

Layer	Material	Thickness [nm]
Superstrate	Glass	Incoherent
Front TCO	ZnO:Al	600
p-layer	p-type a-Si:C:H	15
Absorber layer	intrinsic a-Si:H	290/150
n-layer	n-type a-Si:H	20
Back TCO	GZOa	70
Back reflector	Ag	300

The model was built following the traditional structure of a *pin* cell. Starting from the top of the cell there is the glass superstrate, then the front TCO, then the p-doped, the intrinsic and the n-doped layers, then the back TCO, and finally the back metal reflector. For silicon layers, the thickness used corresponds to the one of the samples provided by FZJ[2]: a 290 nm thick absorber layer of intrinsic a-Si:H, a 15 nm thick p-doped a-Si:C:H layer and a n-doped a-Si:H layer 20 nm thick. The remaining supporting layers thicknesses were determined by considering the optimal values used in thin-film silicon cells [89]. A second set of simulations

---

[1] In order to enforce M-S boundary condition in the created model, it was not possible to build triangular gratings with a vertical side. Hence, to analyse this case a sufficiently small angle (2°) was used.

[2] In the case of n- and p-doped layers, for which FZJ provided two samples with different thickness, the smaller one was considered.

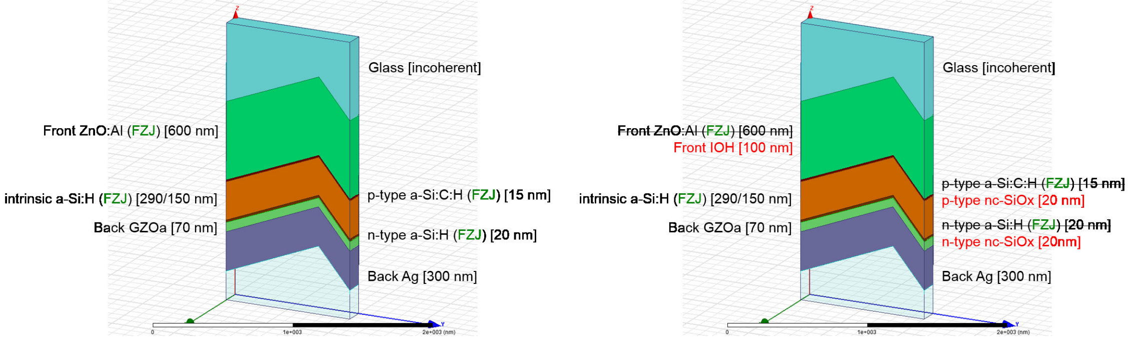

(a) **(b)**

Figure 5-2: 3-D rendering of the simulated unit cells with traditional materials (a) and with optimized materials (b), with thicknesses indicated.

was done employing a thinner amorphous silicon layer (150 *nm*), since real PV cells equipped with such ultra-thin absorber layers suffer less form light-induced degradation, allowing them to perform at the same level (or even better) than thicker cells over their lifetime [93]. In Table 5-1 the material used in the model and their thickness are summarized.

Finally, after the optimal angle of the grating structure was found, two final simulations were ran (one for each absorber layer thickness, using the optimal grating angle previously determined), substituting the front TCO and the doped layers materials used it the previous simulations with better performing materials. In place of ZnO:Al, hydrogenated indium oxide (IOH) was utilized as front TCO. IOH, thanks to its higher electron mobility, can be made thinner than ZnO:Al, while guaranteeing the same electric performance [94]. This, combined with its excellent near-infrared transparency, makes IOH the optimal choice as front TCO for thin-film silicon solar cells. In the simulations, the 600 *nm* thick ZnO:Al was replaced by a 100 *nm* thick IOH layer. The doped layers were also substituted: in place of p-doped a-Si:C:H and n-doped a-Si:H, more transparent p- and n-doped nc-SiO$_x$ layers were used, both having a thickness of 20 *nm*. The difference between the materials used in the traditional and in the optimized cells are presented in Table 5-2 and showed in Figure 5-2.

Table 5-2: Differences between a-Si:H cells with traditional and optimized materials.

Layer	Traditional material (thickness)	Optimized material (thickness)
Front TCO	ZnO:Al (600 *nm*)	IOH (100 *nm*)
p-layer	p-type a-Si:C:H (15 *nm*)	p-type nc-SiO$_x$ (20 *nm*)
n-layer	n-type a-Si:H (20 *nm*)	n-type nc-SiO$_x$ (20 *nm*)

All the models used master-slave boundary conditions on the vertical surfaces of the unit cell, and a Floquet port at the top face. The analysis was conducted for wavelength between 300 *nm* and 1200 *nm*, with steps of 10 *nm*. Since the cell modelled presented a glass superstarte that needs to be incoherent[3],the Floquet port excitation was applied directly of the surface of the (thin) glass layer. The results exported, thus, nedded to be corrected, to include the front reflectance at the air-glass interface. This method of correcting the results after the simulation

---

[3] The real device has a glass carrier with a thickness of *mm*, thus propagation of light inside it is incoherent

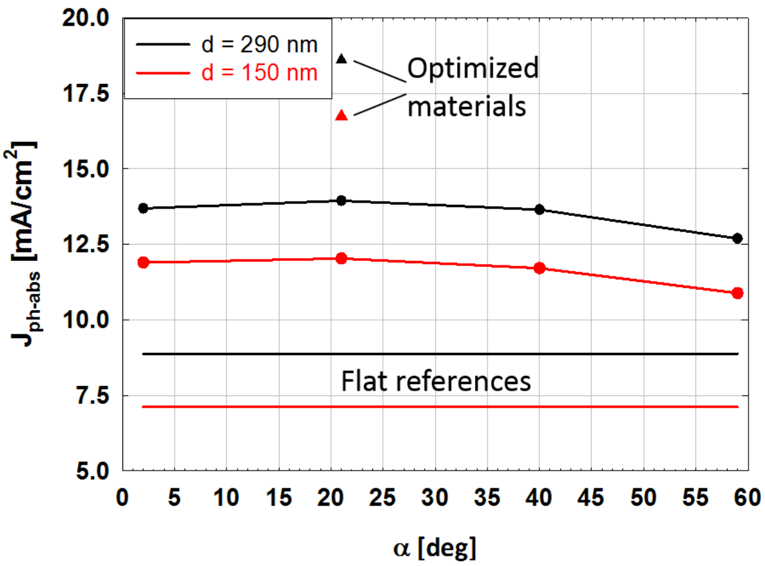

Figure 5-3: Implied photocurrent density generated inside the intrinsic a-Si:H the absorber layer, for flat reference cells, grating devices and structures with optimized materials, as function of the grating inclination α.

was preferred to the alternative of including a very thick glass layer, since this would have greatly increased the simulation time. This reflectance correction was implemented using a MatLab code developed by the PVMD group (thanks to dr. O. Isabella and dr. S. Solntsev). After the correction was done, for each layer of the structure the implied photocurrent densityJ_{ph-i} was calculated and employed as the parameter to compare different structure performances.

5-1-2 Results

The first simulations were ran on flat structures, to have a benchmark to evaluate the performance of the textured devices. The thickness of the layers of this flat references are the same utilized for the solar cells with gratings, in order for the comparison to be meaningful. The results of these first simulations (expressed in terms of implied photocurrent of the absorber layer, J_{ph-abs}) are 8.9 mA/cm^2 for the thicker cell ($d_{abs} = 290\ nm$) and 7.1 mA/cm^2 for the thinner one ($d_{abs} = 150\ nm$).

After the reference structures, two sets of simulations were carried out for the solar cells with gratings, one for each of the two absorber layer thicknesses (290 nm and 150 nm). In both cases the results show similar trends (Figure 5-3): asymmetric gratings perform better than symmetric ($\alpha = 59°$), and the highest J_{ph-abs} values were achieved for a grating inclination α of 21°; these values are, respectively, 13.9 mA/cm^2 ($d_{abs} = 290\ nm$) and 12.0 mA/cm^2 ($d_{abs} = 150\ nm$). The increase achieved with respect to the flat reference cells are +5.0 mA/cm^2 (+ 56.2 %) for the thicker absorber and +4.9 mA/cm^2 (+ 69.0 %) for the thinner. Since the absolute increase is almost equal for both absorber layer thicknesses, the thinner cell is the one that benefits more from presence of the grating (i.e. the relative increase of the performance is higher).

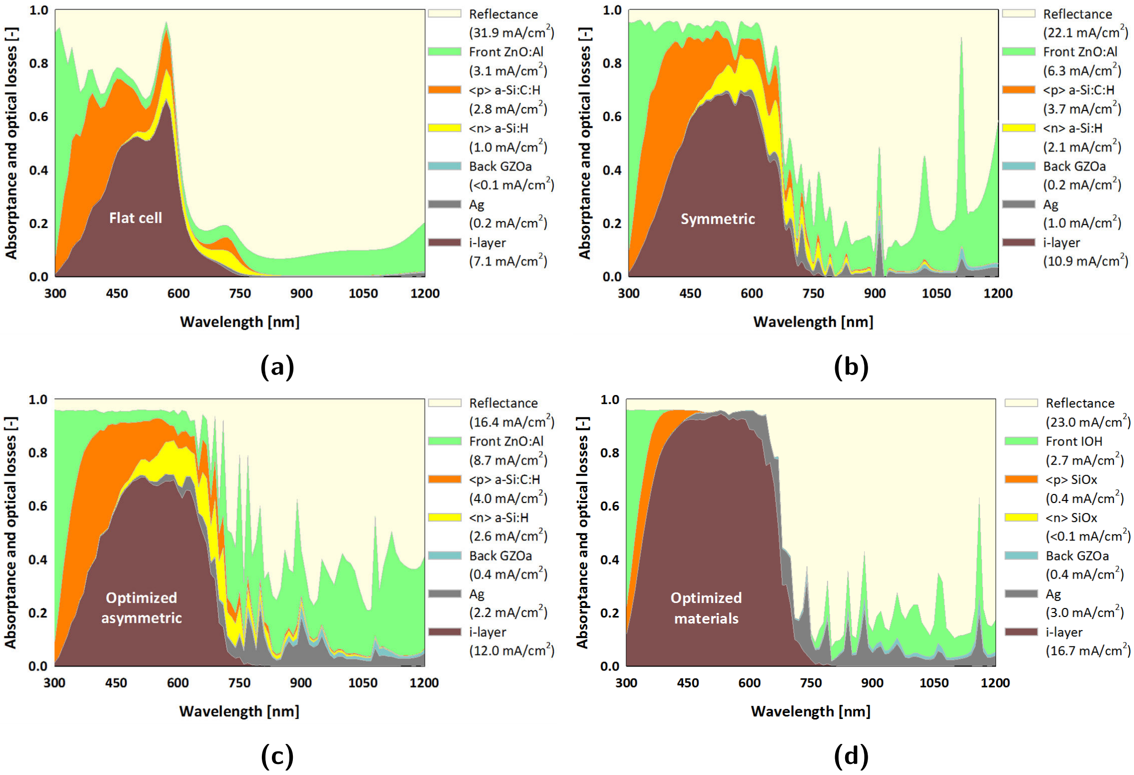

(a) (b)

(c) (d)

Figure 5-4: Simulated i-layer absorptance and optical losses for flat reference cell (a), symmetric grating cell (b), optimized asymmetric grating cell (c) and optimized grating cell with optimal materials (d). All cells have the same a-Si:H absorber layer thickness of 150 nm.

Finally, the simulations with optimal layers (see Figure 5-2b) and optimized inclination $\alpha = 21°$ were carried out. For both absorber layer thicknesses, the adoption of better performing supporting layers resulted in an increase in J_{ph-abs} of $+4.7\ mA/cm^2$ with respect to the structure with optimized grating and standard materials, corresponding to a performance increment of + 33.8 % and + 39.2 %, for the thicker and thinner absorbers respectively.

In Figure 5-4 the simulated i-layer absorptance and the optical losses are shown, for the flat reference, symmetric gratings, optimized asymmetric gratings, and optimal materials, all with $d_{abs} = 150\ nm$. From these plots, the following conclusions can be drawn:

- From the flat reference (Figure 5-4a) to the symmetric grating structure (Figure 5-4b), the reflectance losses reduces considerably, proving the benefit (in terms of primary reflectance reduction) of having textured interfaces and explaining the major increase of J_{ph-abs} achieved.
- Adopting asymmetric gratings (Figure 5-4c) further reduces the reflectance losses, resulting thus in an increased absorption inside the intrinsic (absorber) layer. The reasons for this ulterior reflectance reduction are not yet clear; a possible explanation is that the different geometric configuration generates more multiple reflections between the grating features, giving light more chances of being absorbed inside the device.
- The utilization of optimal materials (Figure 5-4d) have the main benefit of greatly

reducing the parasitic absorption losses inside supporting layers. The increased transparency of these layers results also in an increase of the reflectance, but this drawback is more than compensated by the reduction of the supporting layer losses, resulting in a significant increase of J_{ph-abs} with respect to the standard material case.

In conclusion, the simulations carried out for solar cell devices based on an a-Si:H absorber material showed that asymmetric gratings can outperform equivalent symmetric structures, and that the optimization of the materials used for supporting layers results in a further increase of the performance. In Table 5-3 all the results of this section are summarized.

Table 5-3: Simulated J_{ph-abs} achieved for all simulations with a-Si:H absorbers.

Structure	J_{ph-abs} $[mA/cm^2]$	Increase $[mA/cm^2]$	Relative increase
290 nm absorber			
Flat	8.9	-	-
Symmetric ($\alpha = 59°$)	12.7	+ 3.8	+ 42.7 %
Asymmetric ($\alpha = 40°$)	13.6	+ 4.7	+ 52.8 %
Asymmetric ($\alpha = 21°$)	13.9	+ 5	+ 56.2 %
Asymmetric ($\alpha = 2°$)	13.7	+ 4.8	+ 53.9 %
Opt. materials ($\alpha = 21°$)	18.6	+ 9.7	+ 109.0 %
150 nm absorber			
Flat	7.1	-	-
Symmetric ($\alpha = 59°$)	10.9	+ 3.8	+ 53.5 %
Asymmetric ($\alpha = 40°$)	11.7	+ 4.6	+ 64.8 %
Asymmetric ($\alpha = 21°$)	12.0	+ 4.9	+ 69.0 %
Asymmetric ($\alpha = 2°$)	11.9	+ 4.8	+ 67.6 %
Opt. materials ($\alpha = 21°$)	16.7	+ 9.6	+ 153.2 %

5-2 Micro-crystalline silicon thin-film solar cells

Micro-crystalline silicon is a material of great interest as absorber layer for thin-film solar cells. Compared to amorphous silicon, it shows lower absorption in the visible part of the spectrum (see Figure 2-1)and thus it requires a larger thickness to effectively absorb energy from the solar spectrum. However, its low deposition rate impose small values of the thickness in order to maintain competitive production costs [27]. As a result, state-of-the art μc-Si:H thin-film PV cells have absorber layer thicknesses of only a few micrometers. On the other hand, μc-Si:H has a lower band gap than a-Si:H and can thus can better absorb light in the near infrared (NIR) region. The combination of thicker absorber layers and better NIR absorption allow micro-crystalline silicon thin-film cells to achieve higher values of photocurrent density with respect to a-Si:H devices.

5-2-1 The model

Similarly to what done for the simulations of the a-Si:H structures, the analysis was focused only on the asymmetry of the gratings. Hence, once again the values of the grating period P

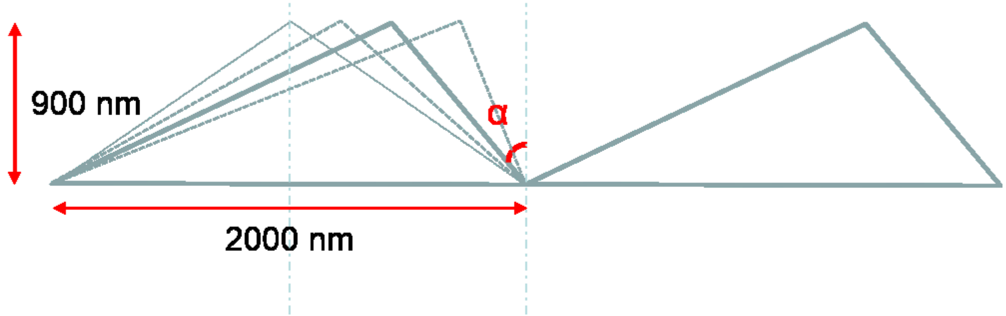

Figure 5-5: Sketch of the μc-Si:H and CIGS solar cell triangular grating cross-sections, indicating period ($P = 2000\ nm$), height ($h = 900\ nm$) and inclination angle α.

and of the grating height h were fixed, this time to 2000 nm and 900 nm respectively (see Figure 5-5). These values were imposed by the Central Glass and Ceramic Research Institute of India, partner of the Delft University of Technology that will realize the substrates for the thin-film cells presented in this chapter. The sweep of the grating inclination was once more done from the symmetric case to the vertical, in four steps: $\alpha = 48°$ (symmetric), $\alpha = 33°$, $\alpha = 18°$, and $\alpha = 3°$ (limit vertical case).

Table 5-4: Structure, materials and relative thicknesses of the μc-Si:H solar cell model using traditional materials.

Layer	Material	Thickness [nm]
Superstrate	Glass	Incoherent
Front TCO	ZnO:Al	600
p-layer	p-type μc-Si:H	30
Absorber layer	intrinsic μc-Si:H	1600/1000
n-layer	n-type μc-Si:H	32
Back TCO	GZOa	70
Back reflector	Ag	300

Once again the structure of a *pin* cell was used, and with the exception of doped and absorber layers, the thicknesses and materials used were the same employed for the modelling of a-Si:H cells (see Table 5-4). The thickness of doped layers were determined by the samples provided by FZJ: a 30 nm thick p-doped μc-Si:H layer and a n-doped μ-Si:H layer 32 nm thick. Two different absorber layer thicknesses were used: for the first set of simulations, the intrinsic μc.Si:H layer was 1600 nm thick, which is the thickness of state-of-the-art devices [27]. In the second set of simulations the absorber layer thickness was 1000 nm, a thickness not sufficient to efficiently absorb photons in the NIR region (unless advanced light management schemes, such as periodic gratings, are implemented) but that would greatly reduce the production costs for this type of cells.

After the optimal inclination α of the gratings was found, simulations with optimized materials were once again carried out. The new materials introduced are the same utilized for the amorphous silicon structure: IOH in place of ZnO:Al as front TCO, p- and n-type silicon-oxide as doped layers instead of p- and n-doped μc-Si:H films. In Table 5-5 the different materials used for the optimized cell are listed.

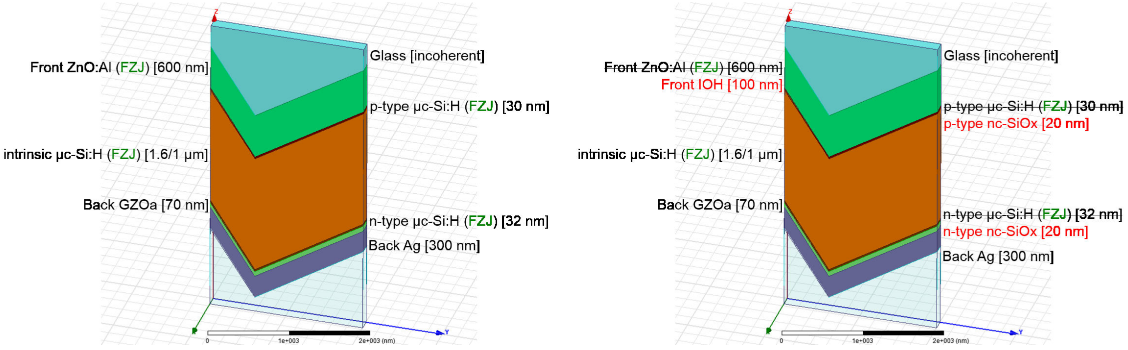

(a) **(b)**

Figure 5-6: 3-D rendering of the unit cells used for the simulation of μc-Si:H-based devices with traditional materials (a) and with optimized materials (b), with thicknesses indicated.

Table 5-5: Differences between μc-Si:H cells with traditional and optimized materials.

Layer	Traditional material (thickness)	Optimized material (thickness)
Front TCO	ZnO:Al (600 nm)	IOH (100 nm)
p-layer	p-type μc-Si:H (30 nm)	p-type nc-SiO$_x$ (20 nm)
n-layer	n-type μc-Si:H (32 nm)	n-type nc-SiO$_x$ (20 nm)

Similarly to the previous simulations for a-Si:H cells, all the models used master-slave boundary conditions on the vertical surfaces of the unit cell, a Floquet port at the top face, and a sweep of wavelengths from 300 nm to 1200 nm with 10 nm steps. After the front reflectance correction was once again done, for each layer of the structure the implied photocurrent densityJ_{ph-i} was calculated and employed as the parameter to compare different structure performances.

5-2-2 Results

To have a comparison benchmark, the first simulations were ran on flat cells that have the same layer thicknesses of the corresponding textured devices. The implied photocurrent densities of the absorber layers (J_{ph-abs}) obtained are 15.3 mA/cm^2 ($d_{abs} = 1600\ nm$) and 13.4 mA/cm^2 ($d_{abs} = 1000\ nm$).

After the reference structures, two sets of simulations were carried out for the solar cells with gratings, one for each of the two absorber layer thicknesses (1600 nm and 1000 nm). Results show the same behaviour (Figure 5-7) observed in a-Si:H structures: asymmetric gratings perform better than symmetric, and the highest J_{ph-abs} values were achieved for a grating inclination α of 18°. The values found are, respectively, 25.4 mA/cm^2 ($d_{abs} = 1600\ nm$) and 23.1 mA/cm^2 ($d_{abs} = 1000\ nm$). The increase achieved with respect to the flat reference cells are +10.1 mA/cm^2 (+ 66.0 %) for the thicker absorber and +9.7 mA/cm^2 (+ 72.4 %) for the thinner. Once more the absolute increase is almost equal for both absorber layer thicknesses, thus the thinner cell is the one that benefits more from presence of the grating (i.e. the relative increase of its performance is higher).

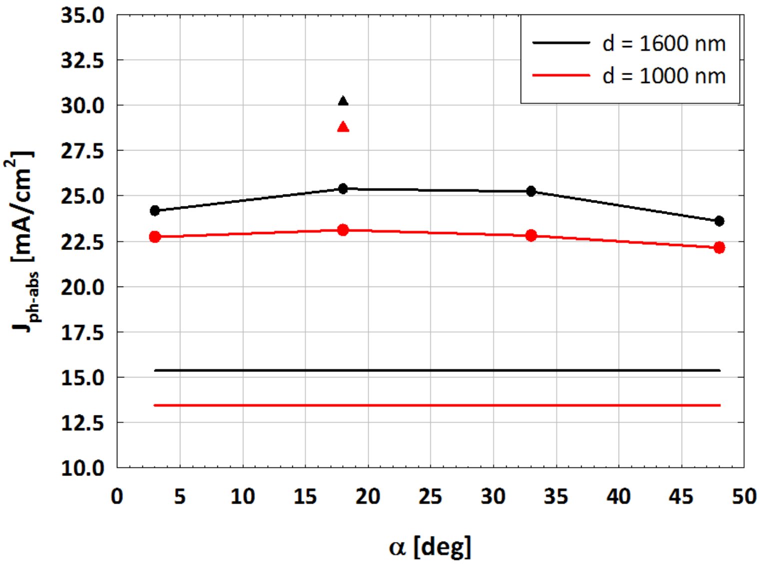

Figure 5-7: Implied photocurrent density generated inside the intrinsic μc.Si:H absorber layer, for flat reference cells, grating devices and structures with optimized materials, as function of the grating inclination α.

Finally, the simulations with optimal layers (see Figure 5-6b) and optimized inclination $\alpha = 18°$ were carried out. The adoption of better performing supporting layers resulted in an increase in J_{ph-abs} of $+4.8\ mA/cm^2$ for the thicker absorber layer (+ 18.9 %) and $+5.7\,mA/cm^2$ for the thinner one (+24.7 %), with respect to the structure with optimized asymmetric gratings but standard materials.

From the plots presented in Figure 5-8 (absorptance and losses for flat, symmetric, asymmetric and optimized cells), the following conclusions can be drawn:

- From the flat reference (Figure 5-8a) to the symmetric grating structure (Figure 5-8b), reflectance at all wavelengths reduces, allowing the textured cell to perform better than the flat one. In particular, the μc-Si absorber layer can greatly benefit from the reduced reflectance in the NIR region of the spectrum, explaining the greater absolute increase in implied photocurrent generated with respect to the case of a-Si:H, that has a very low absorption in the long-wavelength region (see Table 5-3 and Table 5-6).
- Adopting asymmetric gratings (Figure 5-8c) further reduces the reflectance losses (again similarly to the a-Si:H case), resulting thus in an increased absorption inside the intrinsic μc-Si layer.
- The utilization of optimal materials (Figure 5-8d) reduces the parasitic absorption losses inside supporting layers. Once again the front reflectance increases, due to the higher transparency of the optimal materials, but this drawback is more than compensated by the reduction of the supporting layer losses and the resulting J_{ph-abs} is significantly increased.

In conclusion, also the simulation carried out for μc-Si:H based solar cells showed that asymmetric gratings can perform better than symmetric ones, and the optimal angles found in

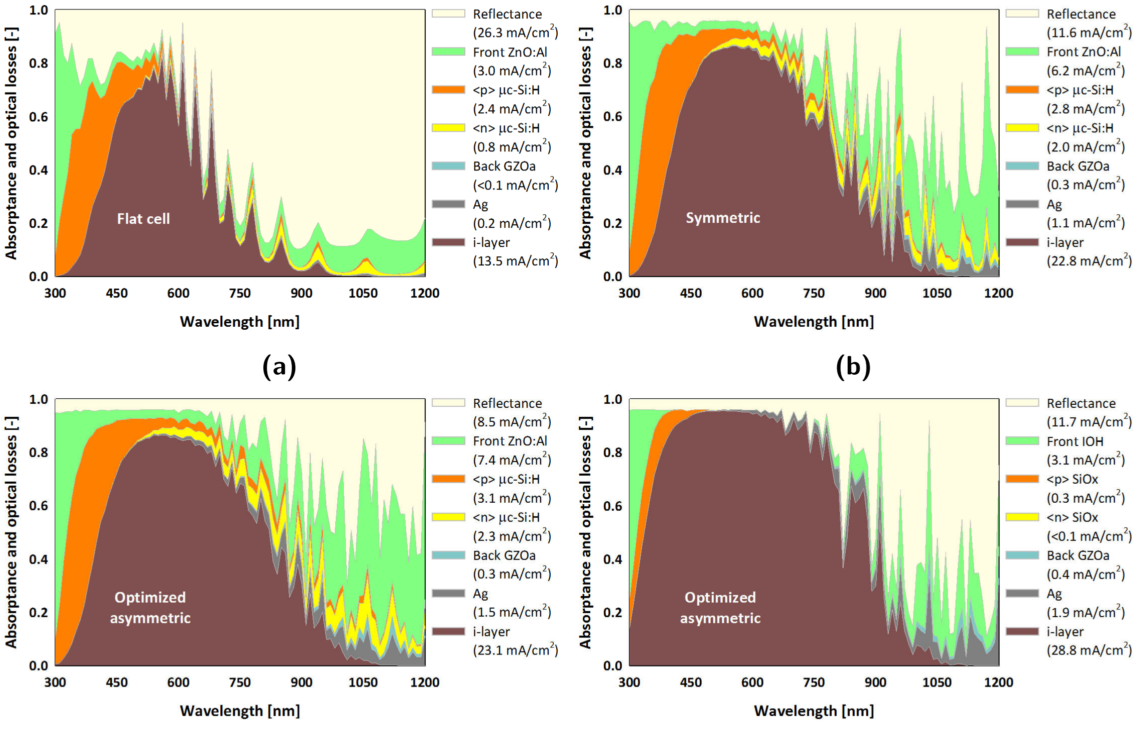

(a) **(b)**

(c) **(d)**

Figure 5-8: Simulated i-layer absorptance and optical losses for flat reference cell (a), symmetric grating cell (b), optimized asymmetric grating cell (c) and optimized grating cell with optimal materials (d). All cells have the same μc-Si:H absorber layer thickness of 1000 nm.

the two cases are very similar (21 ° for a-Si:H and 18 ° for μc-Si:H). The adoption of more performing materials resulted once more in a great improvement of the absorber layer optical performance, with the thinner absorber taking the greatest advantage from this optimization (in both absolute and relative terms). In Table 5-6 the results of the simulations conducted on micro-crystalline silicon devices are summarized.

5-3 CIGS thin-film solar cells

Copper-Indium-Gallium-diSelenide (CIGS) solar cells are among the most promising thin-film PV technologies, particularly because they can achieve high conversion efficiency (around 20 % on laboratory scale [22]) even with small absorber thickness (few μm).

The structure of a conventional CIGS solar cells is the following [27]: over a glass substrate (usually soda-lime glass) a layer of molybdenum is deposited, acting as back reflector and metallic back contact. The CIGS absorber lies directly on top of of the Mo layer, without the presence of a buffer (back) TCO layer as is the case for silicon thin-film devices. Over the absorber are deposited a CdS buffer layer, an intrinsic ZnO film and a ZnO:Al TCO. The main difference between this structure and the *pin* structure of the previously presented thin-film silicon PV cells is the order of deposition of the layers: for CIGS cells the order is from the bottom layer (Mo back contact) to the top one (front TCO), while for *pin* silicon

Table 5-6: Simulated J_{ph-abs} achieved for all simulations with μc-Si:H absorbers.

Structure	J_{ph-abs} $[mA/cm^2]$	Increase $[mA/cm^2]$	Relative increase
1600 nm absorber			
Flat	15.3	-	-
Symmetric ($\alpha = 48°$)	23.6	+ 8.3	+ 54.2 %
Asymmetric ($\alpha = 33°$)	25.2	+ 9.9	+ 64.7 %
Asymmetric ($\alpha = 18°$)	25.4	+ 10.1	+ 66.0 %
Asymmetric ($\alpha = 3°$)	24.2 + 4.8	+ 53.9 %	
Opt. materials ($\alpha = 18°$)	30.2	+ 14.9	+ 97.4 %
1000 nm absorber			
Flat	13.4	-	-
Symmetric ($\alpha = 48°$)	22.1	+ 8.7	+ 64.9 %
Asymmetric ($\alpha = 33°$)	22.8	+ 9.4	+ 70.1 %
Asymmetric ($\alpha = 18°$)	23.1	+ 9.7	+ 72.4 %
Asymmetric ($\alpha = 3°$)	22.7	+ 9.3	+ 69.4 %
Opt. materials ($\alpha = 18°$)	28.8	+ 15.7	+ 119.8 %

cells depositions goes from top (front TCO) to bottom (back Si contact).

State-of-the-art CIGS cells have absorber layers thicknesses between 1500 nm and 2500 nm. While cells with CIGS thicknesses of 2.5 μm and 1.5 μm have similar performance, a further decrease in the absorber thickness results in a quick decrease of the absorptance (i.e. lower short-circuit current densities generated), and thus light management techniques become necessary to maintain high conversion efficiencies values [27]. On the other hand, a decrease of the CIGS thickness would have a great impact on the reduction of both material and production costs of the device. Hence, the reduction of the absorber layer thickness combined with the implementation of light management techniques is the direction to follow in order to reduce the cost of this type of PV cell and to promote its diffusion on a large scale.

5-3-1 The model

Table 5-7: Structure, materials and relative thickness values of the CIGS solar cell model.

Layer	Material	Thickness $[nm]$
Substrate	Soda-lime glass	Incoherent
Back contact	Molybdenum (Mo)	500
Absorber layer	CIGS	2500/600
Buffer layer	CdS	50
TCO buffer	intrinsic ZnO	50
Front TCO	ZnO:Al	500

For this analysis, once again the values of the grating period P and of the grating height h were fixed to 2000 nm and 900 nm respectively (see Figure 5-5), values imposed by the Central Glass and Ceramic Research Institute of India. The sweep of the grating inclination

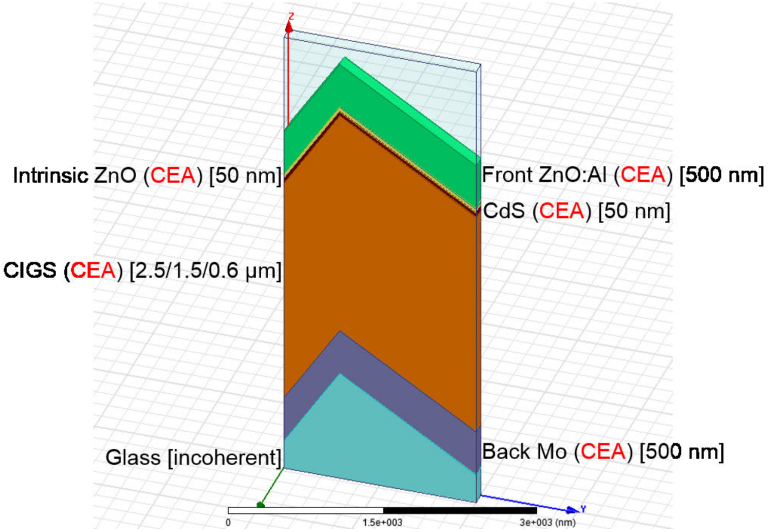

Figure 5-9: 3-D rendering of the unit cells used for the simulation of CIGS-based devices, with values of the thickness indicated.

was once more done from the symmetric case to the vertical, in the same four steps adopted for the μc-Si:H-cell analysis: $\alpha = 48°$ (symmetric), $\alpha = 33°$, $\alpha = 18°$, and $\alpha = 3°$ (limit vertical case).

The thickness of each of the supporting layers (see Table 5-7) corresponds to values of state-of-the-art real devices [27]. The two absorber layer considered were, respectively, 2500 nm thick (standard device) and 600 nm thick (reduced production and material costs). No simulations with more performing materials were carried out, since research has not yet shown the possibility to use other materials than the ones currently employed for CIGS solar cells. In Figure 5-9 the unit cell used for simulations is shown.

Similarly to the previous simulations for silicon thin-film cells, all the models used master-slave boundary conditions on the vertical surfaces of the unit cell. On the other hand, the CIGS models required the presence of a layer of air on top of the structure. Hence, the reflectance correction of simualtion results was not necessary. The analysis was carried out for wavelengths between 300 nm and 1500 nm, with 10 nm steps.

5-3-2 Results

Once again the first simulations were ran on flat cells that have the same layer thickness of the corresponding textured devices. The implied photocurrent densities of the absorber layers (J_{ph-abs}) obtained are 30.7 mA/cm^2 ($d_{abs} = 2500\ nm$) and 26.4 mA/cm^2 ($d_{abs} = 600\ nm$).

After the reference structures performance were evaluated, two sets of simulations were carried out for the textured solar cells, one for each of the two absorber layer thicknesses (2500 nm and 600 nm). Results (Figure 5-10) show that the adoption of gratings improves the implied photocurrent density generated in the absorber layer (although not as strongly as in the case of silicon cells), but the differences between different grating inclinations are very small. The explanation for this behaviour, as well as other considerations on the performance of the models, can be found by looking at the optical losses of the different structures (Figure 5-11):

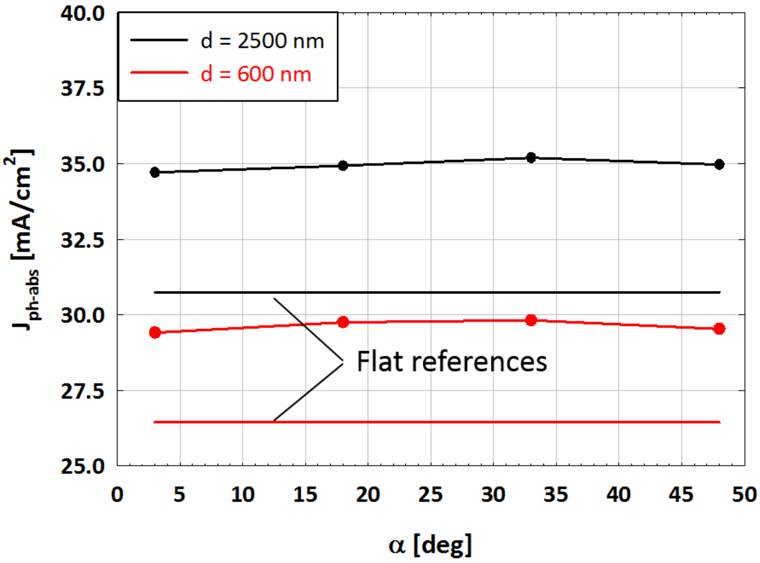

Figure 5-10: Implied photocurrent density generated inside the CIGS absorber layer, for flat reference cells and grating devices, as function of the grating inclination α.

- Symmetric gratings (Figure 5-11b) already reduce the reflectance to very low values, thus the benefits of reduced front reflectance of asymmetric gratings becomes less evident, although still present (see Figure 5-11c and Figure 5-11d).
- The CdS buffer layer is responsible for reduced absorption in the CIGS layer between 400 nm and 500 nm, causing the small "bump" in the absorption curve around 450 nm (Figure 5-11b, Figure 5-11c and Figure 5-11d).
- The front ZnO:Al TCO is a great source of losses at all wavelengths, as was already shown by the simulation on silicon-based cells (where IOH was performing significantly better). At long wavelength though, it is evident that the Mo back reflector is definitely less performing than the corresponding silver reflector used in silicon structures, becoming the main loss source in CIGS textured cells (Figure 5-11b, Figure 5-11c and Figure 5-11d).

In conclusion, simulations carried out for CIGS-based PV cells showed that symmetric and asymmetric gratings have very similar performance, since the presence of such periodic structure (symmetric or asymmetric) reduces almost completely the front reflectance of the device. Moreover, the implied photocurrent densities generated in textured structures with thinner absorber (600 nm) are very close to the corresponding values of flat state-of-the-art flat cells (see Table 5-8), showing that maintaining a high optical performance while reducing the absorber layer thickness is possible when employing periodic gratings.

5-4 Summary of results

The results of all simulations shows that periodic gratings can greatly enhance the optical performance of thin-film solar cells by greatly reducing the primary reflectance of such devices,

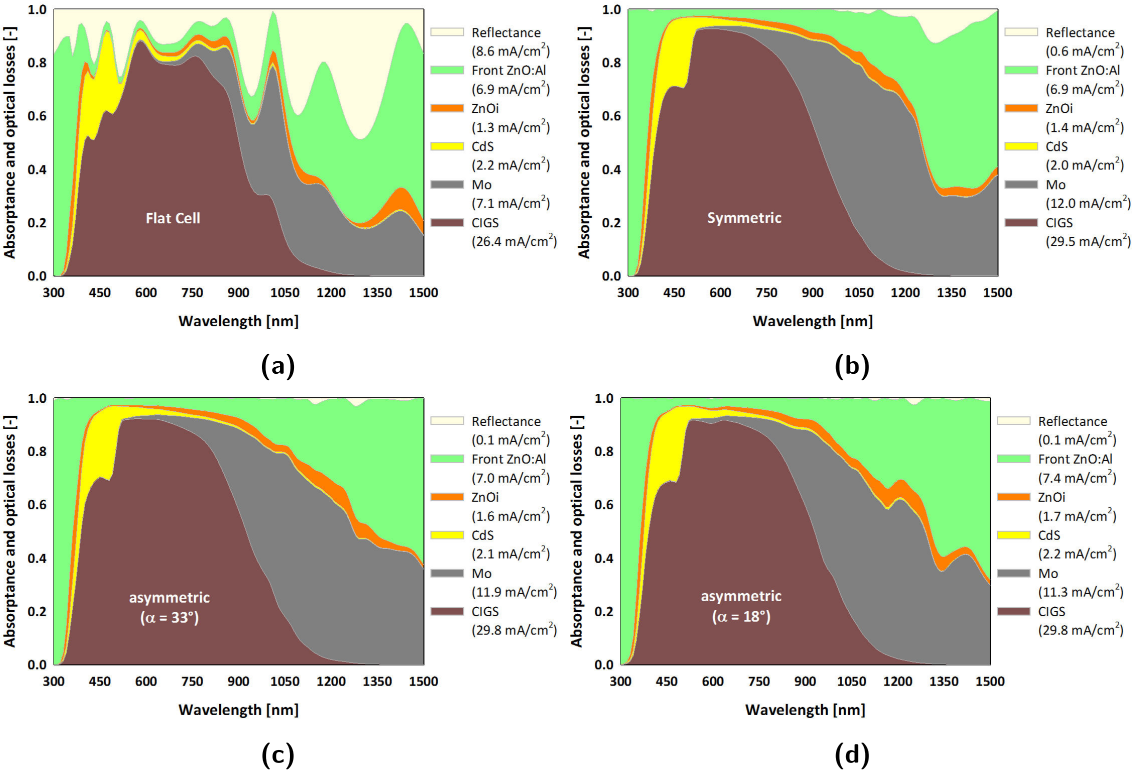

(a) (b)

(c) (d)

Figure 5-11: Simulated i-layer absorptance and optical losses for flat reference cell (a), symmetric grating cell (b), and asymmetric grating cells with $\alpha = 33°$ (c) and $\alpha = 18°$ (d). All cells have the same CIGS absorber layer thickness of 600 nm.

Table 5-8: Simulated J_{ph-abs} achieved for all simulations with μc-Si:H absorbers.

Structure	J_{ph-abs} $[mA/cm^2]$	Increase $[mA/cm^2]$	Relative increase
2500 nm absorber			
Flat	30.7	-	-
Symmetric ($\alpha = 48°$)	35.0	+ 4.3	+ 14.0 %
Asymmetric ($\alpha = 33°$)	35.2	+ 4.5	+ 14.7 %
Asymmetric ($\alpha = 18°$)	34.9	+ 4.2	+ 13.7 %
Asymmetric ($\alpha = 3°$)	34.7 + 4.0	+ 13.0 %	
600 nm absorber			
Flat	26.4	-	-
Symmetric ($\alpha = 48°$)	29.5	+ 3.1	+ 11.7 %
Asymmetric ($\alpha = 33°$)	29.8	+ 3.4	+ 12.9 %
Asymmetric ($\alpha = 18°$)	29.8	+ 3.4	+ 12.9 %
Asymmetric ($\alpha = 3°$)	29.4	+ 3.0	+ 11.4 %

as predicted by theory (see Chapter 2).

The adoption of asymmetric gratings in place of symmetric further reduces the reflectance losses, allowing the absorber layers to generate a higher (implied) photocurrent density. This result is more apparent in silicon-based solar cells, where reflectance losses are generally higher, while for CIGS thin-film structures this effect is less evident (but still present).

Finally, for amorphous and micro/crystalline silicon thin-film cells, the adoption of more transparent material resulted in a further increase of the cell performances. Material optimization for CIGS cells could also enhanced their performance further, especially considering the very high parasitic absorption losses inside supporting layers (in particular front TCO and Mo back contact), but so far no results in that direction have been presented.

Chapter 6

Optical modelling of c-Si solar cells based on elongated nano-structures

In this chapter the results of the modelling of crystalline silicon solar cells based on elongated nano-structures are presented. After the description of the model (Section 6-1), the influence of elongated nano-structures (nanowires) on the propagation of light is analysed (Section 6-2), by considering the effect they have on the electric-field inside the device. This analysis is done to better understand how elongated nano-structures interact with the electromagnetic field and how this interaction affects the performance of silicon solar cells. After this, the geometry of nanowires (NWs) is studied (Section 6-3), with the goal of finding the optimal geometrical configuration that provides the best performance. Finally, the effect of different illumination conditions on the NW cell performance is presented (Section 6-4).

6-1 The radial hetero-junction c-Si nanowire solar cell model

Nanowires have the potential to become a very effective light management technique for thin-film solar cells, since they can eliminate the dichotomy between optical and electrical thickness by orthogonalizing the path of light and charge carriers (see Chapter 2). Despite this potential, nanowire-based solar cells are still outperformed by PV cells that adopt traditional light management schemes. For this reason, an optimization of nanowires must be done in order tu fully exploit their potential.

For this work a crystalline silicon (c-Si) hetero-junction (HTJ) configuration was used. With respect to traditional homo-junction, HTJ used an intrinsic a-Si:H layer to passivate the c-Si surface and achieve better electrical performances [95]. These passivation layer must be very thin (a few *nm*) otherwise it would significantly reduce the cell optical performance by absorbing a large fraction of the incident light.

The structure of the bulk part of the cell corresponds to the *nip* structure of standard crystalline silicon devices; starting from the substrate: a silver back contact/reflector, a back

TCO (gallium-doped zinc oxide GZOa) and the absorber layer, which consists of n-doped c-Si. The nanowires, which are also made of n-doped c-Si, were built directly on top of the bulk c-Si absorber, forming with it a single volume (i.e. there is no interface between bulk c-Si and NWs). The whole structure is then completed by: a passivating intrinsic a-Si:H layer, p-doped nc-SiOx and a front TCO (hydrogenated indium oxide IOH). A list of the layers of the structure with their corresponding (state-of-the-art) thickness employed in the model is presented in Table 6-1.

Table 6-1: Structure, materials and relative thicknesses of the HTJ c-SI NW solar cell model.

Layer	Material	Thickness $[nm]$
Back contact	Ag	300
Back TCO	GZOa	100
Absorber (bulk)	n-doped c-Si	2000
Absorber (NW)	n-doped c-Si	h_{NW}
Passivating layer	intrinsic a-Si:H	5
p-doped layer	p-type nc-SiOx	5
Front TCO	IOH	40

After the layers and their thickness had been decided, the disposition and shape of the nanowires had to be determined. After a brief study, a hexagonal lattice disposition was chosen in favour of a square lattice, since the former provides a better nanowire packing[1], and the cross-section of the nanowires was also chosen to be hexagonal, since it performed better than the alternative circular or square shapes. The geometrical parameters of the NWs are defined as follows (see Figure 6-1):

- The period P is the distance between the axis of two neighbouring nanowires[2].
- The diameter of NWs was defined to be 2 times the apothem a of its hexagonal cross-section.
- The duty cycle d_C was defined as the ration of the diameter $2a$ to the period P ($d_C = 2a/P$).
- The height h of the nanowires is calculated for the internal c-Si nanowire, thus it does not represent the total NW height after the deposition of coating supporting layers.

Simulations were run on a hexagonal unit cell (see Figure 6-2), with appropriately defined master-slave (M-S) boundary conditions and Floquet port excitation. This initial model volume was later reduced by applying PE-PH symmetry conditions (see Chapter 4); in this way the computational time required for each simulation was reduced from the initial 15 hours to around 4 hours. A comparison of the results obtained with the two different models (with and without symmetry boundary conditions) showed that both provided the same results.

---

[1] Considering the same area, there are more nanowires in a hexagonal lattice than in a square or rectangular lattice

[2] Given the hexagonal lattice distribution, every NW is surrounded by 6 NWs

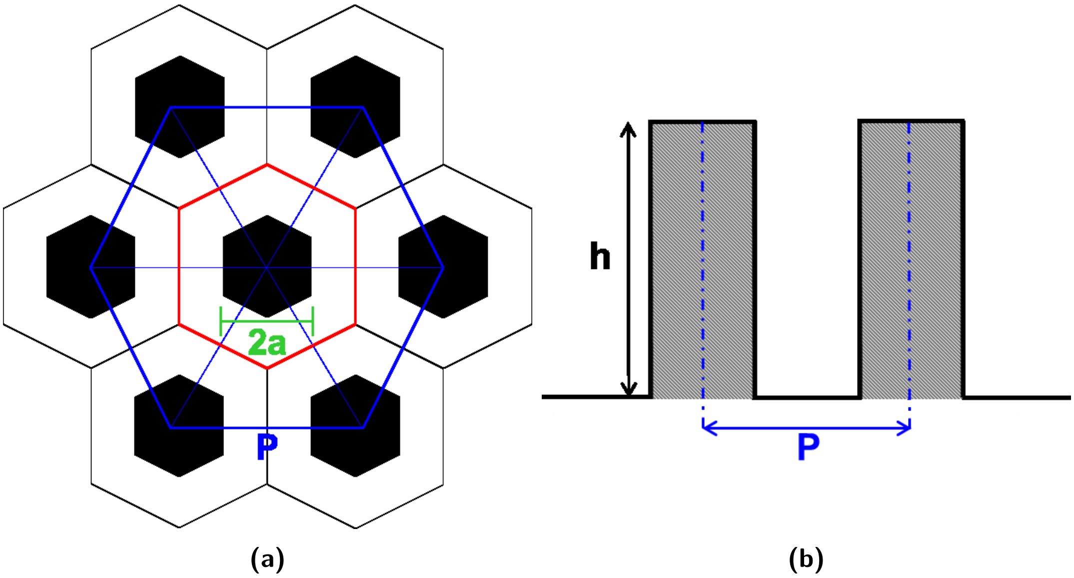

Figure 6-1: Top-view (a) and cross-section (b) sketches of the nanowire array, with period P and nanowire diameter $2a$ and height h indicated.

The analysis was conducted on frequencies between 300 nm and 1200 nm, with 10 nm steps, and the implied photocurrent generated inside the absorber layer (J_{ph-abs}) was once again the quantity used to compare the performance of different structures.

Before presenting the results of simulations, it is useful to analyse how light propagates in nanowire cells, by studying the behaviour of the electric field inside the modelled structures.

6-2 Propagation of light inside c-Si nanowire solar cells

The High Frequency Structure Simulator (HFSS) software can directly calculate the magnitude of the electric field ($|E|$) inside a simulated multi-layer structure; this parameter can be used (in first approximation) to understand how light propagates inside the nanowire solar cell.

For this analysis, a structure with $P = 800$ nm, $h = 2000$ nm and $2a = 200$ nm was used (Figure 6-2). This values correspond to the real geometrical parameters of a hetero-junction c-Si NW cell realized by the PVMD group [96]. The magnitude of the electric field inside the absorber layer was extracted from the simulation results and plotted to graphically understand the light propagation behaviour. The absorptance profile of the c-Si layer was also calculated, and together with the plots of $|E|$ used to analyse the propagation of light inside the solar cell.

In figure Figure 6-4 the absorptance of the nanowire cell is compared to the one of an equivalent flat cell (both with same layer materials and thicknesses). Some considerations can be made:

- At short wavelengths (300-600 nm), the absorptance inside the NW-based cell is lower than in the flat device. The reason for this behaviour is simple: in the NW cell more

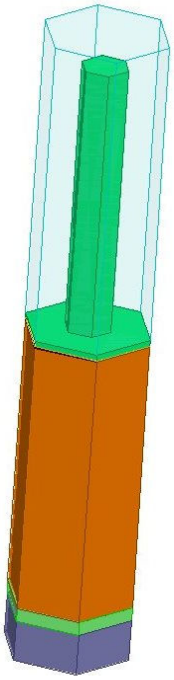

Figure 6-2: 3-D rendering of the hexagonal unit cell model used as reference case for simulations.

material is used for coating layers, since they have to cover a larger area (bulk + NWs). The increase usage of materials results in higher losses inside the supporting layers, explaining thus the reduced cell performance.

- Fabry-Perot resonance peaks (Figure 6-3b), which were already present in the flat solar cell, can still be observed in the NW cell (red arrows). Moreover, at long wavelengths these peaks assume higher values than in the flat cell, suggesting that NWs act as Fabry-Perot amplifiers. These peaks occur at the same wavelengths for both flat and NW cells, since they have the same absorber layer thickness.

- Additional absorptance peaks can be observed for the NW cell (green arrows), clearly caused by the presence of NWs, hence, the presence of NWs induces a wave-guiding effect inside the absorber layer.

In Figure 6-4 the electric field magnitude inside the absorber is plotted, for different wavelengths that correspond to particular cases::

- At 800 nm the magnitude of the electric field (E) is low in both the bulk and the NW, with only small medium intensity regions inside the nanowire. At this wavelength the absorptance has a deep (Figure 6-3b).

- At 820 nm $|E|$ is higher than in the previous case, particularly inside the NW. This explains not only the presence of the FP peak in the absorptance profile, but also its higher value with respect to the flat device.

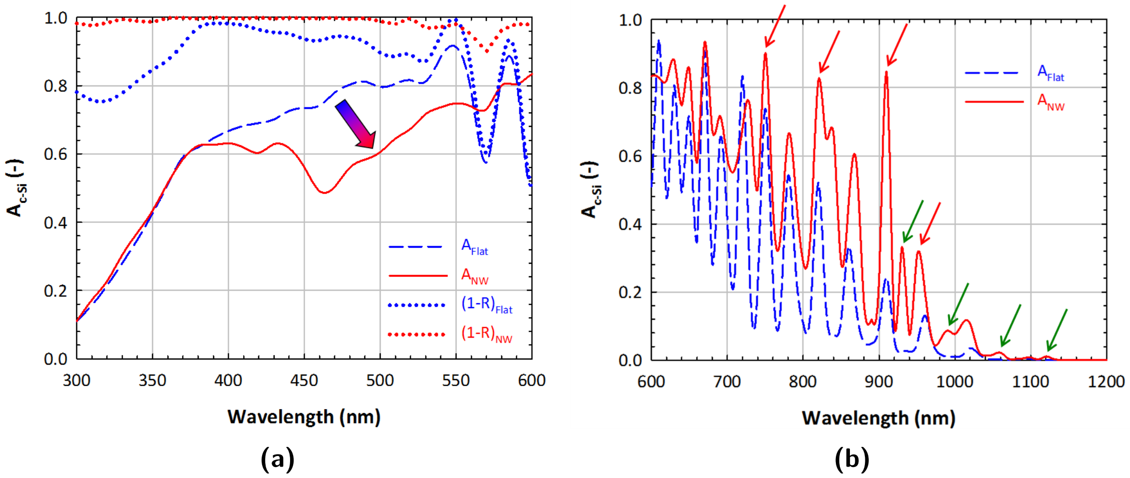

Figure 6-3: Absorptance profiles of a flat and a NW c-Si cells, between 300-600 nm (a) and 600-1200 nm. Fabry-Perot peaks are indicated with red arrows, while additional NW-induced peaks are pointed out by green arrows.

- At 840 nm the magnitude of E inside the bulk is once again low, but there are high intensity regions inside the nanowire. These regions are the reason for the presence of the extra NW-induced peak in the absorptance profile.
- At 960 nm the magnitude of E inside the bulk is shows a lot of high intensity regions, which are excited by the presence of the nanowires, At this wavelength a Fabry-Perot-induced absorptance peak is present, but the excitation induced by the presence of the NW explain its higher value with respect to the flat cell.
- At 1130 nm $|E|$ is particularly high inside the nanowire, while in the bulk the intensity is relatively low. At this wavelength, the absorptance profile shows a NW-induced peak (not caused by Fabry-Perot resonance).

In conclusion, the analysis carried out on the propagation of light inside a NW c-Si solar cells showed that the presence of nanowires contributes to increase the absorptance at longer wavelengths in two different ways: first, they act as Fabry-Perot amplifiers, increasing the values of the absortpance peaks which are already present in the flat cell. Second, at specific wavelengths they induce a wave-guiding effect inside the NWs themselves, resulting in extra absorptance peaks inside the absorber layer of the NW cell. In fact, at wavelengths at which absorptance shows a peak not induced by Fabry-Perot resonances, the electric filed magnitude is high only inside the nanowire. On the other hand, for wavelengths at which Fabry-Perot-induced peaks are induced, $|E|$ has high intensity in both bulk and NW.

6-3 Analysis of the geometrical parameters of nanowire solar cells

After understanding how light propagates inside a NW c-Si solar cell, two series of simulations were carried out to determine the optical behaviour of the model for different NW geometrical

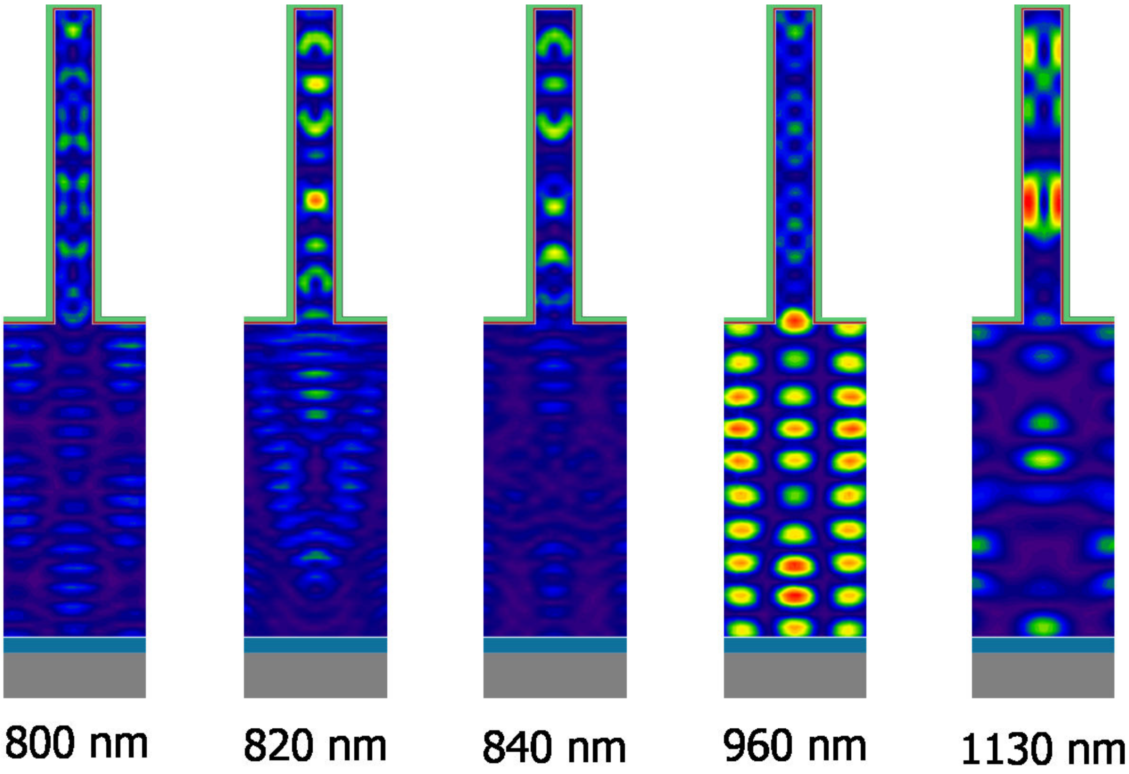

Figure 6-4: Electric field magnitude inside the absorber layer, for different wavelengths.

parameters. In the first series, the influence of the nanowire height h on the absorptance inside the c-Si layer was studied. In the second, the effect of the diameter ($2a$) of nanowires was analysed. For both cases the value of the period P was kept constant at 800 nm. The parameters used for the comparison between the different structure are the implied photocurrent density inside the absorber (J_{ph-abs}), the reflectance losses ($J_{ph-refl}$), and the losses inside supporting layers ($J_{ph-supp}$).

Prior to the geometrical parameters sweep, an equivalent flat cell structure was modelled and simulated, to have a reference case for the analysis; this reference cell has the same layer materials and thicknesses of the corresponding NW cells (for the c-Si absorber layer the flat-cell thickness corresponds to the bulk thickness of the NW device).

6-3-1 Effect of NW height on the optical performance

For this analysis, the value of P and $2a$ were kept constant (at 800 nm and 200 nm), to isolate the effect of the NW height h on the cell performance. The height was swept between 1 μm and 5 μm, with steps of 1 μm (see Table 6-2); an additional simulation with $h = 0.5$ μm was also carried out, while smaller values were not considered, since for relatively low aspect ratios[3] (< 2:1) the nanowire array performs like a 2-D periodic symmetric grating, and thus

---

[3] The aspect ratio is defined as the ratio of a feature height to its horizontal length (in the case of NWs the ratio of h to $2a$). A high aspect ration means very tall and thin features, while a low aspect ratio corresponds to (relatively) flatter structures.

Table 6-2: Values of the height h used in the first simulation series and corresponding values of the implied photocurrent density generated inside the absorber (J_{ph-abs}) and total losses ($J_{ph-refl} + J_{ph-supp}$).

h $[nm]$	J_{ph-abs} $[mA/cm^2]$	$J_{ph-refl} + J_{ph-supp}$ $[mA/cm^2]$
0 (flat)	18.0	28.2
0.5	23.2	23.0
1	22.3	23.9
2	22.0	24.2
3	22.8	23.4
4	22.1	24.0
5	23.2	23.0

its analysis would not be of interest for this work.

In Figure 6-5 the results of this first sweep are presented. From the analysis of the three considered parameters (J_{ph-abs}, $J_{ph-refl}$ and $J_{ph-supp}$), the following conclusions can be drawn:

- The reflectance of the flat cell ($h = 0$ nm) is greatly reduced by using short nanowires ($h = 0.5$ μm), and keeps decreasing when h becomes larger. This result is in accordance with theoretical predictions, since tall features of a textured interface have a stronger anti-reflective effect than short ones.
- On the other hand, taller nanowires employ more material than shorter ones, not only for the absorber, but also for all the coating supporting layers (passivating intrinsic a-Si:H, p-doped nc-SiOx and front TCO layers). Hence, the parasitic absorption in these layers increases almost linearly with h.
- The sum of reflectance and parasitic absorption losses remains (almost) constant for all NW heights, thus the implied photocurrent density generated inside the absorber layer is approximately the same for all values of h (see Table 6-2).

Summarizing, the study of the impact of h on the cell performance shows that the anti-reflective effect achieved by employing taller nanowires is compensated by an increase in parasitic absorption losses; as a result, the NW height does not greatly affect the absorptance inside the c-Si layer (i.e. from an optical point of view, the final performance of the cell does not depend of the NW height).

6-3-2 Effect of NW height on the optical performance

For this second series of simulations, the value of P and h were kept constant (at 800 nm and 2 μm), in order to analyse only the effect of the NW diameter $2a$ on the cell performance. $2a$ was swept between 0 nm (flat cell) and 700 nm, with steps of 50 nm (see Table 6-3) The value of 700 nm represent the limit for the nanowire diameter, since the corresponding diameter of coated nanowires becomes equal to the period P (i.e. the NWs are in conact between each other).

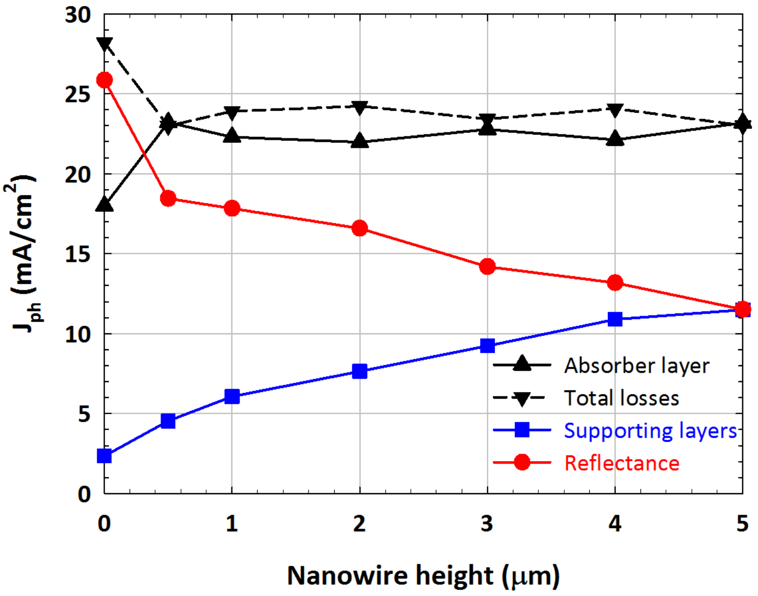

Figure 6-5: Values of the implied photocurrent density J_{ph} (in mA/cm^2) of the absorber, reflectance, losses inside supporting layers and total losses, as function of the NW height h.

In Figure 6-6 the results of the diameter sweep are presented. From the analysis of absorptance (J_{ph-abs}) and losses ($J_{ph-refl}$ and $J_{ph-supp}$), the following conclusions can be drawn:

- The reflectance losses greatly reduce for values of $2a$ from 0 (flat cell) up to 150 nm. A further increase in the NW diameter results in a slower reflectance decrease, until it reaches a minimum at values of the diameter between 350 nm and 450 nm. For larger diameters, the reflectance start to increase again. The optimal diameter values represent the optimal trade-off that reduces the reflectance at the flat bulk surface (which reduces when the NW diameter increases) and the reflectance at the top of the nanowire (which increases for larger diameters).

- When comparing the flat reference to the cells with the thinnest NW diameter (50 nm), it is immediately evident that losses in supporting layers are much higher in the nanowire cell. This can be explained by the fact that the presence on NWs considerably increases the amount of material used, in particular for coating layers (which have to cover a much larger area than in a flat cell). On the other hand, by augmenting the diameter $2a$ further the amount of material used in supporting layers does not increase greatly and parasitic absorption losses remain thus (almost) constant, even showing a tendency to decrease for very large diameters.

- Since the supporting layers losses are approximately constant for all diameters, the maximum absorption is achieved where the reflection has its minimum ($2a = 450nm \Rightarrow d_C = 56.25\%$).

In conclusion, while the nanowire height influences the loss mechanisms, but ultimately does not affect the cell performance (in terms of J_{ph} generated inside the absorber), the NW

Table 6-3: Values of the diameter $2a$, corresponding duty cycles (d_C) used in the second simulation series and obtained results(absorptance J_{ph-abs} and total losses $J_{ph-refl} + J_{ph-supp}$).

$2a$ $[nm]$	d_C [%]	J_{ph-abs} $[mA/cm^2]$	Total losses ($J_{ph-refl} + J_{ph-supp}$) $[mA/cm^2]$
0 (flat)	0	18.0	28.2
50	6.25	16.1	30.0
100	12.50	18.7	27.5
150	18.75	21.2	25.0
200	25.00	21.4	24.8
250	31.25	23.3	22.9
300	37.50	24.6	21.5
350	43.75	25.1	21.1
400	50.00	26.3	19.9
450	56.25	26.8	19.4
500	62.50	26.4	19.8
550	68.75	25.3	20.9
600	75.00	25.2	21.0
650	81.25	24.9	21.2
700	87.50	23.9	22.3

diameter can be optimized to achieve the best performance possible. It is important to note, though, that the value found (450 nm) represents the optimum for a nanowire array with period $P = 800$ nm; for a nanowire cell with an different array period, the optimal diameter will assume a different value.

6-4 Nanowire solar cell performance under different illumination conditions

Finally, an extra series of simulations was carried out, this time to analyse how the nanowire cell performance is affected by different light angles of incidence. To simulate non-perpendicular impinging light, a phase shift between related master and slave boundary surfaces was introduced (see Chapter 4). The structure utilized has an array period of 800 nm and a diameter of 200 nm; various nanowire heights between 0.5 μm and 5 μm were employed, in order to understand how the incident angle affect the cell performance for different values of h. For the comparison, only the implied photocurrent density generated inside the absorber layer was considered.

In total 6 simulations were ran, with light incident angles varying from $0°$ to $75°$ with steps of $15°$. Results are plotted in Figure 6-7 and show that - for all heights - J_{ph-abs} reduces only for very large incident angles ($> 60°$), while in the range between 0 and $60°$ the performance is constant. This particular behaviour is made possible by the particular structure on NW solar cells: while in flat cells wider incident angles result in higer values of relfectance, in the case of NW cells light reflected by the bulk can still be absorbed by the nanowires and thus contirbute to the current generation.

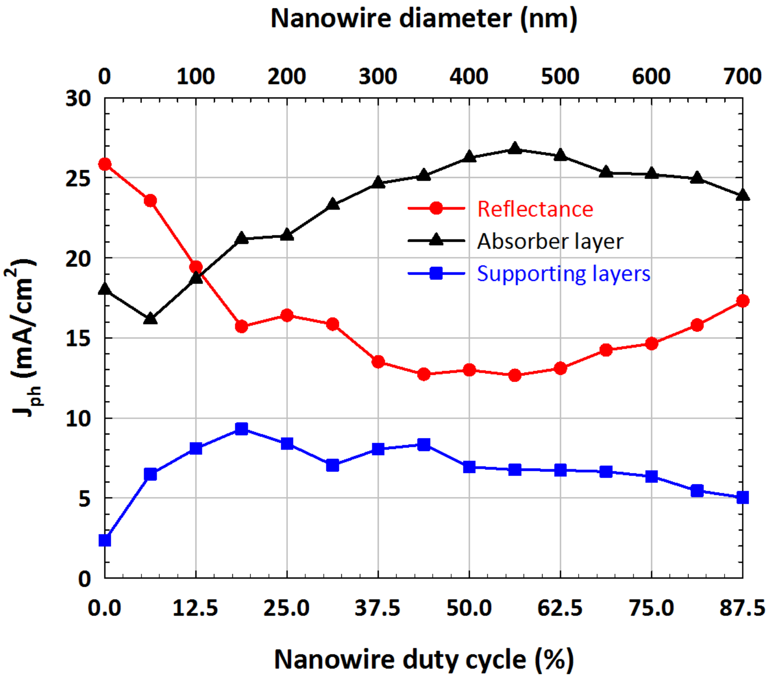

Figure 6-6: Values of the implied photocurrent density J_{ph} (in mA/cm^2) of the absorber, reflectance, losses inside supporting layers and total losses, as function of the NW duty cicle d_C and the diameter $2a$.

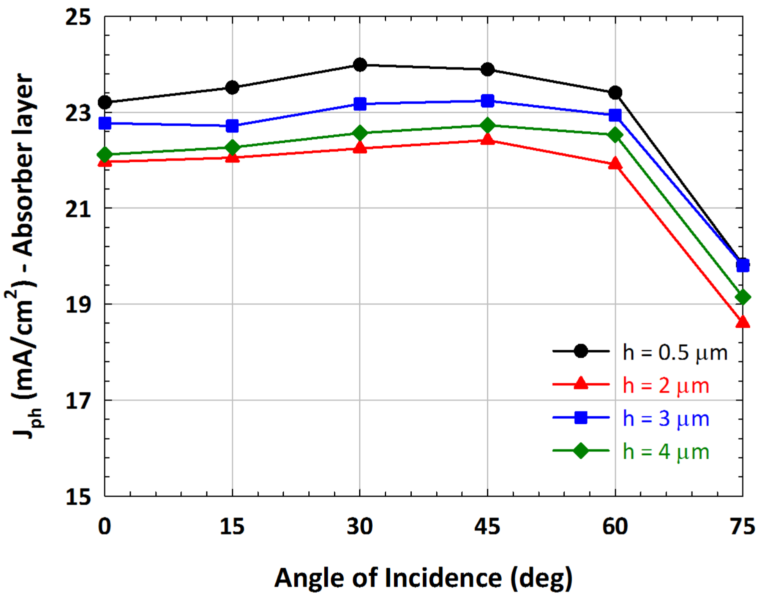

Figure 6-7: Values of the implied photocurrent density J_{ph} inside the absorber layer, for different heights between 0.5 and 5 μm, as function of the light angle of incidence.

6-5 Wrap-up of NW cell simulation results

The simulation work carried out during this project provide a valuable framework to understand the behaviour of elongated nano-structures applied to thin-film silicon solar cells. First, the analysis of light propagation inside the cell showed how the nanowire can increase the absorptance in the long-wavelength region of the spectrum ($\lambda > P$) by acting as Fabry-Perot resonators and exciting wave-guided modes inside the absorber. Then, it was shown that nanowires with different height values have similar performance, while the diameter has a much more evident effect and can thus be optimized. Finally, the study of the NW cells can perform at a constant high level under different illumination conditions, since high values of the implied photocurrent density inside the absorber layer were found for a wide range of light angles of incidence.

Chapter 7

Conclusions and outlook

The aim of this MSc thesis was to investigate the properties and behaviour of materials and structure utilized in thin-film solar cells based on advanced texturization. In this type of PV cells, novel light management techniques are implemented to improve their optical performance and achieve a better *optically thick / electrically thin* trade-off.

After providing a general overview of different photovoltaic technologies and light managements techniques implemented in PV devices, materials commonly used in thin-film solar cells were optically characterized, to extract reliable properties that could then be used as inputs for the simulation work.

The modelling part of this thesis, which was carried out by means of 3-D optical simulations based on the Finite Element Method, represents the core of this project and consisted of a thorough analysis of different advanced structures that can be used to enhance the optical performance of thin-film PV cells. This investigation was divided in 2 parts: (i) study and optimization of various thin-film technologies based on 1-D periodic asymmetric triangular gratings and (ii) evaluation of the optical behaviour of different elongated nano-structures (also called nanowires) applied to crystalline silicon based hetero-junction thin-film solar cells.

In the first part, the analysis was carried out for devices based on a-Si:H, μc-Si:H and CIGS absorber materials. Results show that asymmetric gratings have a stronger anti-reflective effect than symmetric textures, for all three absorber materials. This effect is more evident for silicon-based solar cells, where reflectance losses are generally higher. In the case of CIGS, the implementation of gratings (symmetric or asymmetric) already reduces the total reflectance losses to very low values, and thus the performance difference between symmetric and asymmetric structures is very small. The optimal value of the grating inclination α for all three thin-film cell models was found: $\alpha = 21°$ for a-Si:H, $\alpha = 18°$ for μc-Si and $\alpha = 33°$ for CIGS.

A material optimization was also carried out, only for the silicon cell models (since for CIGS devices alternatives to the traditionally employed materials have not yet been found). By utilizing more transparent doped layers, and a thinner and less absorbing TCO that can guarantee high electrical conductivity values, the optical performance of a-Si:H and muc-Si:H textured solar cells was further increased, allowing very thin absorbers to achieve relatively high values of generated implied photocurrent.

The second part of the project was focussed on the analysis of nanowires. First, an investigation on the light propagation mechanism inside nanowire solar cells based on c-Si absorbers was carried out. The results of this study showed that nanowire can greatly increase the c-Si layer absorptance at wavelengths longer than the array period, by acting as Fabry-Perot amplifiers and by exciting wave-guided modes inside the absorber.
After the interaction between light and nanowires was understood, the analysis turned to the optimization of the geometrical parameters of the elongated nano-structures. Maintaining constant the nanowire shape, array distribution and distance (i.e. constant value of the array period P), the effect of height and diameter was studied. Results show that the cell optical performance remains constant for height values between 0.5 μm and 5 μm, since the decrease in primary reflection achieved by taller nanowires is compensated by an increase in parasitic absorption losses. On the other hand, the supporting layer losses are approximately the same for nanowire diameter values between 50 nm and 700 nm. Hence, the implied photocurrent density generated inside the absorber layer reached a maximum where the reflectance losses were at a minimum; the optimal diameter was found to be $2a = 450\ nm$.
Finally, the investigation of the nanowire solar cell performance for different light angle of incidence showed that this type of device can maintain a high performance level for a wide range of incident angles (between 0 and 60°).

Regarding the analysis of gratings for thin-film devices, the following research topics could be of interest to further enhance the optical performance:

- Analysis of 2-D symmetric and asymmetric pyramidal gratings.
- Study of modulated periodic textures (1-D and 2-D).
- Utilization of better performing materials (non-metallic back contacts for silicon cells, alternative TCO and back reflector materials for CIGS devices, ...).

Further development is also necessary in the case of simulations of solar cells based on nanowires:

- An analysis of the interaction between light and different types of nanowires is necessary in order to completely understand how the presence of nanowires affect the optical performance of a photovoltaic solar cell.
- A study of the effect of different geometrical parameters (array period, nanowire inclination) or configurations (tapered and/or modulated nanowires) is desirable, in order to achieve a full optimization of nanowire solar cells.

Bibliography

[1] U.S. Energy Information Administration (EIA), "International Energy Outlook," 2013.

[2] International Energy Agency (IEA), "World Energy Outlook. Executive Summary," 2013.

[3] International Energy Agency (IEA), "Energy Supply Security," 2014.

[4] D. H. Meadows, D. L. Meadows, J. Randers, and W. W. Behrens III, *The Limits to Growth.* Universe Books, 1972.

[5] Intergovernmental Panel on Climate Change (IPCC), *Climate Change 2013: The Physical Science Basis. Contribution of Working Group I to the Fifth Assessment Report of the Intergovernmental Panel on Climate Change.* Cambridge University Press, 2013.

[6] International Energy Agency (IEA), "Key World Energy Statistics," 2013.

[7] International Energy Agency (IEA), "World Energy Investment Outlook," 2014.

[8] International Energy Agency (IEA), "Deploy Renewables 2011: Best and Future Policy Practice," 2011.

[9] T. A. Boden, G. Marland, and R. Andres, "Global, Regional, and National Fossil-Fuel CO2 Emissions," tech. rep., Carbon Dioxide Information Analysis Center, Oak Ridge National Laboratory, U.S. Department of Energy, Oak Ridge, Tenn., U.S.A., 2010. (doi 10.3334/CDIAC/00001_V2010).

[10] V. Smil, "Energy at the Crossroads," tech. rep., Organisation for Economic Co-operation and Development (OECD), 2006.

[11] International Energy Agency (IEA), "Soalr Enegry Perspectives: Executive Summary," 2011.

[12] D. E. Carr, *Energy & the Earth Machine.* W. W. Norton & Company, 1976.

[13] K. Branker, M. Pathak, and J. Pearce, "A review of solar photovoltaic levelized cost of electricity," *Renewable and Sustainable Energy Reviews*, vol. 15, pp. 4470–4482, 2011.

[14] M. Bazilian, I. Onyeji, M. Liebreich, I. MacGill, J. Chase, J. Shah, D. Gielen, D. Arent, D. Landfear, and S. Zhengrong, “Re-considering the Economics of Photovoltaic Power ,” *Renewable Energy*, vol. 53, 2013.

[15] R. Williams, “Becquerel Photovoltaic Effect in Binary Compounds,” *The Journal of Chemical Physics*, vol. 32, May 1960.

[16] S. J. Fonash and R. T. Fonash, “Solar cell,” *Encyclopædya Britannica*. (Available online at http://www.britannica.com/EBchecked/topic/552875/solar-cell/. Retreived 2014-05-19).

[17] D. M. Bagnall and M. Boreland, “Photovoltaic technologies,” *Energy Policy*, vol. 36, pp. 4390–4396, 2008.

[18] M. Green, *Third-Generation Photovoltaics: Advanced Solar Energy Conversion*. Springer, Berlin, 2006.

[19] W. Shockley and H. J. Queisser, “Detailed Balance Limit of Efficiency of p-n Junction Solae Cells,” *Journal of Applied Physics*, vol. 32, no. 3, pp. 510–519, 1961.

[20] G. Conibeer, “Third-generation photovoltaics,” *materialstoday*, vol. 10, pp. 42–50, November 2007.

[21] International Renewable Energy Agency (IRENA), “Solar Photovoltaics,” June 2012. (Renewable Energy Technologies: Cost Analysis Series; Volume 1: Power Sector, Issue 4/5).

[22] M. A. Green, K. Emery, Y. Hishikawa, W. Warta, and E. D. Dunlop, “Solar cell efficiency tables (version 43),” *Progress in Photovoltaics*, vol. 22, pp. 1–9, 2014.

[23] D. C. Jordan and S. R. Kurtz, “Photovoltaic Degradation Rates - An Analytical Review,” 2014. (To be published in Progress in Photovoltaics: Research and Applications. Available at http://www.nrel.gov/docs/fy12osti/51664.pdf. Retrieved on 2014-08-11).

[24] National Renewable Energy Laboratory (NREL), “Best Research-Cell Efficiencies.” (Available at http://www.nrel.gov/. Retrieved on 2014-08-11.

[25] European Photovoltaic Industry Association (EPIA), “Solar Generation 6: Solar Photovoltaic Electricity Empowering the World,” 2011.

[26] M. A. Green, “Self-consistent optical parameters of intrinsic silicon at 300K ncluding temperature coefficients,” *Solar Energy Materials & Solar Cells*, vol. 92, pp. 1305–1310, 2008.

[27] “Collaborative Project AGATHA: Project Proposal Part B,” 2010.

[28] “http://rredc.nrel.gov/solar/spectra/am1.5/. Retreived on 2014-08-15.”

[29] “Absorption coefficient.” Available at http://rredc.nrel.gov/solar/spectra/am1.5/. Retreived on 2014-08-15.

[30] M. A. Alama and M. Ryyan Khan, “Fundamentals of PV efficiency interpreted by a two-level model,” *American Journal of Physics*, vol. 49, pp. 35–44, December 1997.

[31] O. Isabella, *Light management in thin-film silicon solar cells.* PhD thesis, Delft University of Technology, January 2013.

[32] Meier, S. Dubail, R. Platz, P. Torres, U. Kroll, J. Anna Selvan, N. P. Vaucher, C. Hof, D. Fischer, H. Keppner, R. Flückiger, A. Shah, V. Shklover, and K. D. Ufert, "Towards high-efficiency thin-film silicon solar cells with the 'micromorph' concept," *Solar Energy Materials and Solar Cells*, vol. 81, pp. 655–662, September 2013.

[33] J. Yang and S. Guha, "Double-junction amorphous silicon-based solar cells with 11% stable efficiency," *Applied Physics Letters*, vol. 61, no. 24, pp. 2917–2919, 1992.

[34] W. Guter, J. Schöne, S. P. Philipps, M. Steiner, G. Siefer, A. Wekkeli, E. Welser, E. Oliva, A. W. Bett, and F. Dimroth, "Current-matched triple-junction solar cell reaching 41.1% conversion efficiency under concentrated sunlight," *Applied Physics Letters*, vol. 94, no. 22, 2009.

[35] J. Yang, A. Banerjee, and S. Guha, "Triple-junction amorphous silicon alloy solar cell with 14.6% initial and 13.0% stable conversion efficiencies," *Applied Physics Letters*, vol. 70, no. 22, pp. 2975–2977, 1997.

[36] M. Stan, D. Aiken, B. Cho, A. Cornfeld, V. Ley, P. Patel, P. Sharps, and T. Varghese, "High-efficiency quadruple junction solar cells using {OMVPE} with inverted metamorphic device structures," *Journal of Crystal Growth*, vol. 312, no. 8, pp. 1370 – 1374, 2010.

[37] A. V. Shah, M. Vaněček, J. Meier, F. Meillaud, J. Guillet, D. Fischer, C. Droz, X. Niquille, S. Faÿ, E. Vallat-Sauvain, V. Terrazzoni-Daudrix, and J. Bailat, "Basic efficiency limits, recent experimental results and novel light-trapping schemes in a-Si:H, μc-Si:H and 'micromorph tandem' solar cells," *Journal of Non-Crystalline Solids*, vol. 338 – 340, no. 0, pp. 639 – 645, 2004.

[38] J. Krč, F. Smole, and M. Topic, "Optical simulation of the role of reflecting interlayers in tandem micromorph silicon solar cells," *Solar Energy Materials and Solar Cells*, vol. 86, no. 4, pp. 537 – 550, 2005.

[39] A. Bielawny, J. ÃIJpping, P. T. Miclea, R. B. Wehrspohn, C. Rockstuhl, F. Lederer, M. Peters, L. Steidl, R. Zentel, S.-M. Lee, M. Knez, A. Lambertz, and R. Carius, "3d photonic crystal intermediate reflector for micromorph thin-film tandem solar cell," *physica status solidi (a)*, vol. 205, no. 12, pp. 2796–2810, 2008.

[40] L. Zeng, P. Bermel, Y. Yi, B. A. Alamariu, K. A. Broderick, J. Liu, C. Hong, X. Duan, J. Joannopoulos, and L. C. Kimerling, "Demonstration of enhanced absorption in thin film si solar cells with textured photonic crystal back reflector," *Applied Physics Letters*, vol. 93, no. 22, 2008.

[41] A. Barnett, D. Kirkpatrick, C. Honsberg, D. Moore, M. Wanlass, K. Emery, R. Schwartz, D. Carlson, S. Bowden, D. Aiken, A. Gray, S. Kurtz, L. Kazmerski, M. Steiner, J. Gray, T. Davenport, R. Buelow, L. Takacs, N. Shatz, J. Bortz, O. Jani, K. Goossen, F. Kiamilev, A. Doolittle, I. Ferguson, B. Unger, G. Schmidt, E. Christensen, and D. Salzman, "Very high efficiency solar cell modules," *Progress in Photovoltaics: Research and Applications*, vol. 17, no. 1, pp. 75–83, 2009.

[42] D. Ginley, M. A. Green, and R. Collins, "Solar energy conversion toward 1 terawatt," *MRS Bulletin*, vol. 33, pp. 355–364, April 2008.

[43] S. Fischer, A. Ivaturi, B. Frohlich, M. Rudiger, A. Richter, K. Krämer, B. Richards, and J. Goldschmidt, "Upconverter silicon solar cell devices for efficient utilization of sub-band-gap photons under concentrated solar radiation," *IEEE Journal of Photovoltaics*, vol. 4, pp. 183–189, Jan 2014.

[44] G. E. Arnaoutakis, J. Marques-Hueso, A. Ivaturi, K. W. Krämer, S. Fischer, J. C. Goldschmidt, and B. S. Richards, "Enhanced up-conversion for photovoltaics via concentrating integrated optics," *Optics Express*, vol. 22, pp. A452–A464, Mar 2014.

[45] A. Boccolini, J. Marques-Hueso, D. Chen, Y. Wang, and B. Richards, "Physical performance limitations of luminescent down-conversion layers for photovoltaic applications," *Solar Energy Materials and Solar Cells*, vol. 122, no. 0, pp. 8 – 14, 2014.

[46] A. Nozik, "Quantum dot solar cells," *Physica E: Low-dimensional Systems and Nanostructures*, vol. 14, no. 1–2, pp. 115 – 120, 2002.

[47] R. P. Raffaelle, S. L. Castro, A. F. Hepp, and S. G. Bailey, "Quantum dot solar cells," *Progress in Photovoltaics: Research and Applications*, vol. 10, no. 6, pp. 433–439, 2002.

[48] M. Green, *Solar cells: operating principles, technology, and system applications.* Englewood Cliffs, NJ, Prentice-Hall, Inc.

[49] J. Krč, F. Smole, and M. Topic, "Advanced optical design of tandem micromorph silicon solar cells," *Journal of Non-Crystalline Solids*, vol. 352, no. 9 – 20, pp. 1892 – 1895, 2006.

[50] T. Fujibayashi, T. Matsui, and M. Kondo, "Improvement in quantum efficiency of thin film si solar cells due to the suppression of optical reflectance at transparent conducting oxide/si interface by tio2/zno antireflection coating," *Applied Physics Letters*, vol. 88, May 2006.

[51] R. Vismara, "Effect of Periodic Texturing on Thin-Film Solar Cells: Analysis of optical properties for 1-D periodic gratings," October 2013. (SIP II project for the MSc in Sustainable Energy Technology at TU Delft).

[52] H. Fujiwara and M. Kondo, "Effects of carrier concentration on the dielectric function of ZnO:Ga and $In_2O_3 : Sn$ studied by spectroscopic ellipsometry: Analysis of free-carrier and band-edge absorption," *Physical Review B*, Feb 2005.

[53] S. Faÿ, J. Steinhauser, N. Oliveira, E. Vallat-Sauvain, and C. Ballif, "Opto-electronic properties of rough lp-cvd zno:b for use as {TCO} in thin-film silicon solar cells," *Thin Solid Films*, vol. 515, no. 24, pp. 8558 – 8561, 2007.

[54] C. Battaglia, C.-M. Hsu, K. Söderström, J. Escarré, F.-J. Haug, M. CharriÃÍre, M. Boccard, M. Despeisse, D. T. L. Alexander, M. Cantoni, Y. Cui, and C. Ballif, "Light trapping in solar cells: Can periodic beat random?," *ACS Nano*, vol. 6, no. 3, pp. 2790–2797, 2012.

[55] H. Sai, H. Fujiwara, M. Kondo, and Y. Kanamori, "Enhancement of light trapping in thin-film hydrogenated microcrystalline si solar cells using back reflectors with self-ordered dimple pattern," *Applied Physics Letters*, vol. 93, no. 14, 2008.

[56] M. D. Kelzenberg, S. W. Boettcher, J. A. Petykiewicz, D. B. Turner-Evans, M. C. Putnam, E. L. Warren, J. M. Spurgeon, R. M. Briggs, and H. A. Lewis, Nathan S.Atwater, "Enhanced absorption and carrier collection in Si wire arrays for photovoltaic applications," *Nature Materials*, vol. 9, no. 3.

[57] V. E. Ferry, M. A. Verschuuren, M. C. v. Lare, R. E. I. Schropp, H. A. Atwater, and A. Polman, "Optimized spatial correlations for broadband light trapping nanopatterns in high efficiency ultrathin film a-si:h solar cells," *Nano Letters*, vol. 11, no. 10, pp. 4239–4245, 2011.

[58] E. Yablonovitch, "Statistical ray optics," *Journal of the Optical Society of America*, vol. 72, pp. 899–907, Jul 1982.

[59] Z. Yu, A. Raman, and S. Fan, "Fundamental limit of nanophotonic light trapping in solar cells," *Proceedings of the National Academy of Sciences*, 2010.

[60] A. Naqavi, F.-J. Haug, K. Söderström, C. Battaglia, V. Paeder, T. Scharf, H. P. Herzig, and C. Ballif, "Angular behavior of the absorption limit in thin film silicon solar cells," *Progress in Photovoltaics: Research and Applications*, 2013.

[61] A. Naqavi, F.-J. Haug, C. Battaglia, H. P. Herzig, and C. Ballif, "Light trapping in solar cells at the extreme coupling limit," *Journal of the Optical Society of America B*, vol. 30, pp. 13–20, Jan 2013.

[62] J. N. Munday, D. M. Callahan, and H. A. Atwater, "Light trapping beyond the 4n2 limit in thin waveguides," *Applied Physics Letters*, vol. 100, no. 12, 2012.

[63] Y. Kuang, M. Di Vece, J. K. Rath, L. van Dijk, and R. E. I. Schropp, "Elongated nanostructures for radial junction solar cells," *Reports on Progress in Physics*, vol. 76, no. 10, p. 106502, 2013.

[64] L. Tsakalakos, J. Balch, J. Fronheiser, B. A. Korevaar, O. Sulima, and J. Rand, "Silicon nanowire solar cells," *Applied Physics Letters*, vol. 91, no. 23, 2007.

[65] E. Garnett and P. Yang, "Light Trapping in Silicon Nanowire Solar Cells," *Nano Letters*, vol. 10, no. 3, pp. 1082–1087, 2010.

[66] E. C. Garnett and P. Yang, "Silicon Nanowire Radial p-n Junction Solar Cells," *Journal of the American Chemical Society*, vol. 130, no. 29, pp. 9224–9225, 2008.

[67] T. Stelzner, M. Pietsch, G. Andrä, F. Falk, E. Ose, and S. Christiansen, "Silicon nanowire-based solar cells," *Nanotechnology*, vol. 19, no. 29, p. 295203, 2008.

[68] A. Fontcuberta i Morral, J. Arbiol, J. Prades, A. Cirera, and J. Morante, "Synthesis of Silicon Nanowires with Wurtzite Crystalline Structure by Using Standard Chemical Vapor Deposition," *Advanced Materials*, vol. 19, no. 10, pp. 1347–1351, 2007.

[69] Garnett, Erik C. and Brongersma, Mark L. and Cui, Yi and McGehee, Michael D., “Nanowire solar cells,” *Annual Review of Materials Research*, vol. 41, no. 1, pp. 269–295, 2011.

[70] K.-Q. Peng and S.-T. Lee, “Silicon Nanowires for Photovoltaic Solar Energy Conversion,” *Advanced Materials*, vol. 23, no. 2, pp. 198–215, 2011.

[71] C. Colombo, M. Heiß, M. Grätzel, and A. Fontcuberta i Morral, “Gallium arsenide p-i-n radial structures for photovoltaic applications,” *Applied Physics Letters*, vol. 94, no. 17, 2009.

[72] E. Uccelli, J. Arbiol, C. Magen, P. Krogstrup, E. Russo-Averchi, M. Heiss, G. Mugny, F. Morier-Genoud, J. Nygård, J. R. Morante, and A. Fontcuberta i Morral, “Three-dimensional multiple-order twinning of self-catalyzed gaas nanowires on si substrates,” *Nano Letters*, vol. 11, no. 9, pp. 3827–3832, 2011.

[73] P. Krogstrup, H. I. Jorgensen, M. Heiss, O. Demichel, J. V. Holm, M. Aagesen, J. Nygård, and A. Fontcuberta i Morral, “Single-nanowire solar cells beyond the Shockley-Queisser limit,” *Nature Photononics*, vol. 7, pp. 306–310, april 2013.

[74] S. Geißendörfer, M. Vehse, T. Voss, J.-P. Richters, B. Hanke, K. von Maydell, and C. Agert, “Integration of n-doped zno nanorod structures as novel light-trapping concept in amorphous thin film silicon solar cells,” *Solar Energy Materials and Solar Cells*, vol. 111, no. 0, pp. 153 – 159, 2013.

[75] R.-E. Nowak, M. Vehse, O. Sergeev, T. Voss, M. Seyfried, K. von Maydell, and C. Agert, “Zno nanorods with broadband antireflective properties for improved light management in silicon thin-film solar cells,” *Advanced Optical Materials*, vol. 2, no. 1, pp. 94–99, 2014.

[76] K. Peng, Y. Xu, Y. Wu, Y. Yan, S.-T. Lee, and J. Zhu, “Aligned single-crystalline si nanowire arrays for photovoltaic applications,” *Small*, vol. 1, no. 11, pp. 1062–1067, 2005.

[77] V. Sivakov, G. AndrÃď, A. Gawlik, A. Berger, J. Plentz, F. Falk, and S. H. Christiansen, “Silicon Nanowire-Based Solar Cells on Glass: Synthesis, Optical Properties, and Cell Parameters,” *Nano Letters*, vol. 9, no. 4, pp. 1549–1554, 2009.

[78] E. P. A. M. Bakkers, J. A. van Dam, S. De Franceschi, L. P. Kouwenhoven, M. Kaiser, M. Verheijen, H. Wondergem, and P. van der Sluis, “Epitaxial growth of InP nanowires on germanium,” *Nature Materials*, vol. 3, pp. 769–773, Nov 2004.

[79] G. Demésy and S. John, “Solar energy trapping with modulated silicon nanowire photonic crystals,” *Journal of Applied Physics*, vol. 112, no. 7, 2012.

[80] K. Jäger, O. Isabella, L. Zhao, and M. Zeman, “Light scattering properties of surface-textured substrates,” *physica status solidi (c)*, vol. 7, no. 3-4, pp. 945–948, 2010.

[81] *CompleteEASE Software Manual. Data acquisition and Analysis Software for J.A. Woollam Co. Spectroscopic Ellipsometers*, Oct 2011.

[82] “http://www.jawoollam.com/tutorial$_1.html.Retreivedon2014 - 08 - 17.''$

[83] “http://www.fz-juelich.de/portal/EN/Home/home$_node.html.''$

[84] “http://www.cea.fr/english-portal.”

[85] A. Čampa, *Modelling and optimization of advanced optical concepts in thin-film solar cells.* PhD thesis, University of Ljubljana, 2009.

[86] J.A. Sap and O. Isabella and K. Jäger and M. Zeman, “Extraction of optical properties of flat and surface-textured transparent conductive oxide films in a broad wavelength range,” *Thin Solid Films*, vol. 520, no. 3, pp. 1096 – 1101, 2011.

[87] D. Schroder, R. Thomas, and J. Swartz, “Free Carrier Absorption in Silicon,” *Solid-State Circuits, IEEE Journal of*, vol. 13, pp. 180–187, Feb 1978.

[88] A. Yariv and P. Yeh, *Optical Waves in Crystals.* John Wiley & Sons, 1984.

[89] O. Isabella, S. Solntsev, D. Caratelli, and M. Zeman, “3-d optical modeling of thin-film silicon solar cells on diffraction gratings,” *Progress in Photovoltaics: Research and Applications*, vol. 21, no. 1, pp. 94–108, 2013.

[90] I. Bardi, R. Remski, D. Perry, and Z. Cendes, “Plane wave scattering from frequency-selective surfaces by the finite-element method,” *Magnetics, IEEE Transactions on*, vol. 38, pp. 641–644, Mar 2002.

[91] D. Kröner, “Plane wave scattering from frequency-selective surfaces by the finite-element method,” *Mathematics of Computation*, vol. 57, pp. 153–167, 1991.

[92] “Ansys HFSS 12, HFSS online help, Technical notes.”

[93] M. Zeman, “Simulation of the maximum possible efficiency of a-Si:H based solar cell neglecting SWE.” 2^{nd} International Workshopof Thin Film Silicon Solar Cells IWTFSSC - April 21-23 2009, Berlin, Germany.

[94] C. Battaglia, L. Erni, M. Boccard, L. Barraud, J. Escarré, and S

[95] “http://pvlab.epfl.ch/heterojunction_solar_cells.”

[96] R. Vismara, O. Isabella, A. Ingenito, F. T. Si, and M. Zeman, “Radial heterojunction c-si nanowire solar cells with 11.8% conversion efficiency.” (Submitted to the ACS Nano journal), Sep 2014.

Glossary

List of Acronyms

1G	1^{st} generation
2G	2^{nd} generation
3G	3^{rd} generation
AID	angular intensity distribution
AR	anti-reflective
ARC	anti-reflective coating
ARTA	Automated Reflectance/Transmittance Analyzer
CEA	Commissariat á l'Energie Atomique
CIGS	Copper-Indium-Gallium-diSelenide
CIS	Copper-Indium-Selenide
DSSC	dye-sensitized solar cells
EIA	U.S. Energy Information Administration
EPIA	European Photovoltaic Industry Association
FEM	Finite Element Method
FZJ	Forschungszentrum Jülich GmbH
GHG	greenhouse gasses
GZOa	gallium-doped zinc oxide
HFSS	High Frequency Structure Simulator
HTJ	hetero-junction

IEA	International Energy Agency
IOH	hydrogenated indium oxide
IPCC	Intergovernmental Panel on Climate Change
IRENA	International Renewable Energy Agency
IS	Integrating Sphere
NIR	near infrared
NREL	National Renewable Energy Laboratory
NWs	nanowires
OECD	Organisation for Economic Co-operation and Development
PV	photovoltaics
PVMD	Photovoltaic Materials and Devices
RAM	random access memory
SEM	scanning electro microscope
TCO	transparent conducting oxide
TF	thin-film
TU Delft	Delft University of Technology
UV	ultraviolet

List of Symbols

$\alpha(\lambda)$	Absorption coefficient
$\delta_p(\lambda)$	Penetration depth
$\kappa(\lambda)$	Extinction coefficient
λ	Wavelength
$\Phi(\lambda)$	Photon flux
$\mathbf{E}$	Electric field
$\mathbf{H}$	Magnetic field
μc-Si	Micro-crystalline silicon
$\tilde{n}(\lambda)$	(Complex) Refractive index
FF	Fill-factor
$H_R(\lambda)$	Haze of reflected light
$H_T(\lambda)$	Haze of transmitted light

h	Height
$I(z,\lambda)$	Intensity of light
J_{ph}	Implied photocurrent density
J_{sc}	Short-circuit current density
$n(\lambda)$	Refractive index
P	Grating period
q	Elementary charge
$R_D(\lambda)$	Diffused reflectance
$R_T(\lambda)$	Total reflectance
$T_D(\lambda)$	Diffused transmittance
$T_T(\lambda)$	Total transmittance
V_{oc}	Open-circuit voltage
a-Si	Amorphous silicon
Ag	Silver
c-Si	Crystalline silicon
CdS	Cadmium-Sulfide
CdTe	Cadmium-Telluride
GaAs	Gallium-Arsenide
InP	Indium-Phosphide
mc-Si	Multi-crystalline silicon
Mo	Molybdenum
Si	Silicon
ZnO:Al	Aluminum-doped zinc-oxide
Wp	Watt-peak
\$	US Dollars

Index